

Force Sensors Constructed from Ferromagnetic Particles Embedded Within Soft Materials

By

Justin K. Ruffalo

B.S., University of Kansas, 2018

Submitted to the graduate degree program in Bioengineering and the Graduate Faculty of the
University of Kansas in partial fulfillment of the requirements
for the degree of Master of Science.

Chair: Cory Berkland, Ph.D.

Elizabeth Friis, Ph.D.

Mei He, Ph.D.

Date Defended: 19 May 2020

The thesis committee for Justin K. Ruffalo certifies that this is the
approved version of the following thesis:

Force Sensors Constructed from Ferromagnetic Particles
Embedded Within Soft Materials

Chair: Cory Berkland, Ph.D.

Date Approved: 19 May 2020

Abstract

The inclusion of magnetic particles as fillers within soft materials has the potential to drive the development of smart materials with high functionality and structural diversity. Six ferromagnetic fillers (i.e., nickel, carbonyl iron, cobalt, iron oxide, magnetite, and neodymium powder) were incorporated within polydimethylsiloxane at concentrations of 0.01 wt %, 0.1 wt %, and 1 wt %. Defined compression tests determined the ability to detect material deformation and the magnetic field response generated during compression cycles. Utilizing iron oxide at 1 wt %, the compressive response of additional silicones and a two-part polyurethane was also investigated.

Compression testing of five of the six ferromagnetic fillers in PDMS, with the exception of carbonyl iron, revealed that 1 wt % was the minimum concentration required to detect compression events via the magnetic field response. The findings of carbonyl iron at 1 wt % were not viable as its magnetic field response was similar to that of the PDMS control samples. The neodymium filler particles produced the strongest magnetic field response. However, settling of the neodymium particles became evident during the curing process, which prompted further theoretical exploration at various particle sizes and viscosities. Our findings suggested that smaller neodymium particle sizes should be explored in future analyses. PDMS displayed the optimal relationship between force and displacement amongst the various polymers with 1 wt % iron oxide. The other materials were either too soft or were too resistive to be considered viable as a durable soft sensor material or were limited by an inability to measure magnetic field strength.

Acknowledgments

I would like to express my sincere gratitude to my advisor, committee members, parents and friends. All of them have provided me with the courage to complete this research and the tenacity to complete this report.

Thank you to my advisor Dr. Cory Berkland at the University of Kansas for not only giving me the incredible opportunity to work with him in the laboratory but also for becoming a friend and a mentor. He maintained an incredible amount of confidence in me as well as has provided me with on-going guidance and encouragement. He has provided me with a laboratory experience that I'm not soon to forget as I carry on in my career.

I also owe a significant amount of gratitude to my laboratory partners, Jon Whitlow, Sebastian Huayamares, and Bryce Stottlemire for their unrelenting patience with this process. To my friends including all of my other laboratory colleagues, thanks for journeying with me through this wild adventure and providing me with lots of helpful feedback and constructive criticism. I would also like to acknowledge the financial support that was provided for this work by Dr. Berkland and the University of Kansas as well as the Honeywell Corporation for making this important research a reality.

Last but not the least, an immeasurable thanks are owed to my parents for their unflinching support. Their unconditional love and support which have always been with me, even when we are thousands of miles apart. This would not have been possible without you!

Table of Contents

Abstract	iii
Acknowledgments.....	iv
List of Figures	vii
List of Tables	xi
Chapter 1: Background	1
Introduction.....	1
Collaborative Data	5
State of the Art Summary and Objectives	11
Chapter 2: Compression Testing of Ferromagnetic Particles Within Soft Materials	13
Introduction.....	13
Materials & Methods	15
Nickel Nanorod Synthesis.....	15
Remaining Magnetic Materials.....	15
Characterization	16
Soft Materials.....	16
Preparation of Samples	17
Compression Testing and Sensing	19
Statistical Analysis.....	21
Results & Discussion	22
Conclusions.....	42
Chapter 3: Future Directions.....	44
References.....	47

Appendix..... 50

List of Figures

Figure 1: 3D printing of NuSil R40-2181 in an EnvisionTEC 3D-Bioplotter.....	6
Figure 2: Extrusion tests of nickel nanorods in NuSil R40 at 0.1, 1, and 10 wt %. The scale bars are equal to 20 μm	6
Figure 3: Microscope imaging of 1 wt % (small = 1-4 μm [left], medium = 4-8 μm [middle], and large = 8-12 μm [right]) nickel nanorods in NuSil R40.	7
Figure 4: Viscoelasticity of 1 wt % medium and large nickel nanorods within NuSil R40.	7
Figure 5: Directional mechanical testing of 1 wt % horizontal and vertically aligned medium (4-8 μm) PDMS-nickel nanorod constructs.....	8
Figure 6: Compressive modulus as a function of magnetic field strength of 1 wt % horizontal and vertically aligned medium (4-8 μm) PDMS-nickel nanorod constructs.....	9
Figure 7: Quantitative sensing of PDMS and NuSil R40 cushions with 1 wt % nickel nanorods.	10
Figure 8: Changes in magnetic field strength in 1 wt % horizontal and vertically aligned PDMS-nickel nanorods constructs at various compression intervals.	10
Figure 9: Magnetic field response from the x, y, and z axis of a 1 wt % PDMS-nickel nanorod construct during different magnitudes of displacement.....	11
Figure 10: A) Vacuum chamber for removing air bubbles prior to placing samples in oven. B) Samples with electromagnet mounted perpendicularly inside curing oven set at 70 $^{\circ}\text{C}$	18
Figure 11: Experimental setup of compression testing. A) Cylindrical sample is placed on top of magnetometer and top geometry of ElectroForce 5500 is lowered to sample height until contact is made. B) Theoretical graph of force (g) versus time (s) showing the incremental steps of 200 g of force applied at 20 g/s for steps i, ii, and iii, and the removal of 200 g of force applied during	

steps iv, v, and vi. C) Theoretical figure of a cylinder being compressed or recovered during each incremental step of applied force over the course of 140 s..... 20

Figure 12: A) Custom built stepper motor to perform preliminary studies B) Compression geometry of stepper motor i) NEMA-23 2 phase stepper motor ii) Motor controller with A4988 stepper motor driver and iii) LSM303 triple-axis accelerometer and magnetometer iv) Sensor controller v) Cylindrical sample to be compressed..... 21

Figure 13: A) Nickel nanorods, B) carbonyl iron microspheres, C) cobalt nanowires D) iron(II,III) oxide (FeO and Fe₂O₃) nanopowder, E) magnetite (Fe₃O₄) powder F) neodymium iron boron powder. The scale bars are equal to 10 mm. 23

Figure 14: All six ferromagnetic materials at 0.01 wt % (Left), 0.1 wt % (Middle), and 1 wt % (Right) within PDMS. A) Nickel, B) carbonyl iron C) cobalt D) iron oxide, E) magnetite, and F) neodymium. 24

Figure 15: A) Blank samples of 2-part polyurethane (Left), DMS-V21 (Middle-Left), DMS-V33 (Middle-Right), and PDMS (Right). B) Samples each containing 1 wt % iron oxide. 24

Figure 16: Magnetic field strength (displayed from the z-axis) and the force versus time of a 1 wt % sample of nickel..... 25

Figure 17: Magnetic field strength from all six magnetic fillers at 1 wt % during 0, 200, 400, and 600 g of force. * denotes statistical difference from PDMS at 600 g of force (p < 0.0001). 27

Figure 18: Magnetic field strength (displayed from the z axis) and the displacement versus time of the same 1 wt % sample of nickel depicted in Figure 16. 28

Figure 19: Displacement of all six magnetic fillers at 1 wt % during 0, 200, 400, and 600 g of force. 29

Figure 20: Displacement as a function of force of the same 1 wt % nickel sample seen in Figure 16..... 30

Figure 21: Displacement as a function of force for one sample (n=1) of each magnetic material at 1 wt % within PDMS. Only the compression cycles are displayed here. 30

Figure 22: Magnetic field strength as a function of displacement for one sample (n=1) of each magnetic material at 1 wt % within PDMS. Only the compression cycles are displayed here. ... 31

Figure 23: Preliminary results of field strength (displayed from the z axis) and the displacement versus time of 1 wt % nickel. 32

Figure 24: Magnetic field strength from materials studied during preliminary trials at 1 wt % during 0, 0.75, 1.50, and 2.25 mm of displacement..... 33

Figure 25: Magnetic field strength of all six magnetic fillers at 0.01, 0.1, and 1 wt % during 600 g of force. * denotes statistical difference from PDMS at 1 wt % and at 600 g of force ($p < 0.0001$). 34

Figure 26: Displacement of all six magnetic fillers at 0.01, 0.1, and 1 wt % during 600 g of force. 35

Figure 27: Magnetic field strength of blank soft materials and soft materials with 1 wt % iron oxide during 0, 200, 400, and 600 g of force. * denotes statistical difference from PDMS Blank at 600 g of force ($p < 0.03$). 37

Figure 28: Displacement of blank soft materials and soft materials with 1 wt % iron oxide during 0, 200, 400, and 600 g of force. 37

Figure 29: Displacement as a function of force for one sample (n=1) of each soft material with and without 1 wt % iron oxide. Only the compression cycles are displayed here. 38

Figure 30: Estimated settling velocities of magnetic particles within solutions of varying viscosities.....	40
Figure 31: Estimated settling velocities of differing particle sizes (1, 25, 50, 75, and 100 nm) of neodymium within solutions of varying viscosities.....	41
Figure 32: Magnetic field strength from all six magnetic fillers at 0.1 wt % during 0, 200, 400, and 600 g of force.	50
Figure 33: Displacement of all six magnetic fillers at 0.1 wt % during 0, 200, 400, and 600 g of force.	51
Figure 34: Magnetic field strength from all six magnetic fillers at 0.01 wt % during 0, 200, 400, and 600 g of force.	51
Figure 35: Displacement of all six magnetic fillers at 0.01 wt % during 0, 200, 400, and 600 g of force.	52
Figure 36: Magnetic field strength as a function of force for one sample (n=1) of each magnetic material at 1 wt % within PDMS. Only the compression cycles are displayed here.	52

List of Tables

Table 1: Comparison of various wearable technologies for rehabilitation glove (***) Desirable, ** Nominal, * Worst)9.	4
Table 2: Physical properties of ferromagnetic materials.	16
Table 3: Physical properties of uncured soft materials.	17
Table 4: Estimated mixture densities and viscosities of silicones at 15:1 w/w ratio with Sylgard 184 curing agent.....	39
Table 5: Volume % of ferromagnetic fillers within PDMS at each wt %.	42
Table 6: Vol % of iron oxide within each soft material.....	42

Chapter 1: Background

Introduction

An entirely new class of electronic devices known as stretchable electronics and specifically soft sensors that can be placed in textiles are the focus of a number of research opportunities. These devices have applications in wearable electronics, human-machine interfaces, and in soft exosuits and robotics¹. On-going investigations have been performed to determine the characteristics (i.e., sensitivity) of soft sensing materials that are somehow (i.e., patterned onto, attached to, or encapsulated within) incorporated into a polymer or other type of matrix^{1, 2}. Further investigations have sought to combine the utilities of wireless human motion detection with self-healing properties³. To date, the state of the art in electromagnetic sensing has focused on the materials utilized, their capacity to detect compression, their sensitivity, various means of measurement, durability, and accuracy.

A variety of materials and techniques have been studied in the development of soft sensors. Approximately 5 years ago, Frutiger and colleagues described how they devised a textile-mounted, capacitive soft strain sensor fibers for the detection of elongational strains using a multicore-shell printing approach¹. Their findings indicated that the soft sensors produced accurate and hysteresis-free performance in both static and dynamic operating conditions. The authors further suggested that these sensors could be readily integrated with textiles^{4, 5} and may have a wide range of wearable-sensor applications including the capacity to capture the gate cycle of a wearer in real time.

The printing of polymers for the development of soft sensors has been accomplished typically through extrusion-based methods. In recent years, the utilization of three-dimensional (3D) printing represents one of the most effective ways to manufacture customized parts with

significant complexity. Additive manufacturing techniques, such as 3D printing, that combine real-time colloidal assembly with existing additive manufacturing technologies to create highly programmable discontinuous fiber composites have been evaluated^{6,7}. Discontinuous fiber composites are unique in that they represent a class of materials that are strong, lightweight and have remarkable fracture toughness². In the investigation by Martin and colleagues (2015), a 3D magnetic printing process was utilized to recreate complex, bioinspired reinforcement architectures that delivered enhanced material performance as compared to monolithic structures. Overall, they found that 3D magnetic printing was promising as a new manufacturing tool to design the micro-architecture of reinforced composites to maximize material properties but felt that printing speeds could be improved upon. They also noted that printed composite materials demonstrate clear mechanical dependence upon their underlying micro-architecture through harness mapping and tensile testing.

The utilization of 3D printing was also applied to conductive self-healing hydrogels, a class of novel materials mimicking human skin and having applicability in human motion detection^{3,8}. These materials may have the ability to change the trajectory of the industrial process due to their potential applications in soft robotics, biomimetic prostheses, and health monitoring systems. In their process the investigators printed the self-healing hydrogel on an ammonium per sulfate (APS) contained gelatin membrane (the sacrificial layer), which was then placed on a thin polydimethylsiloxane (PDMS) membrane from the printed side with another PDMS membrane used to cover the 3D printed pattern. They considered the sensing performance, the 3D printability and the stretchability of the developed material to offer superior functionalities as compared to previously investigated materials³.

Wearable technologies, such as gloves, have also been investigated as a method of accurately measuring hand joint angles and rehabilitation progress in individuals with hand deformities and those suffering from disorders such as rheumatoid arthritis and carpal tunnel syndrome⁹. These “gloves” are often categorized as those that are stretch sensor-based, those that are magnetic sensor-based, those that are Hall effect based. Other categories include vision-based, accelerometer-based, and flex-sensor based. Each of these categories have advantages and limitations seen in Table 1⁹. Briefly, flex-sensors suffer from repeatability issues and a decrease in accuracy over time; accelerometer-based sensors require careful placement of the sensors (challenging due to the fixed shape and dimensions of the accelerometers); vision-based technologies require high performance computational resources (e.g., processing speeds and memory); stretch-sensor based technologies may have errors and inconsistencies due to gaps in the material components and the knit structure affecting their duration of use; and magnetic sensor technologies suffer from changes in sensitivity with changes in their size and their slower response time as compared to other sensors (i.e., accelerometers and flex sensors)⁹.

Among the various sensor types, Hall effect sensors have the advantage of being of low cost, are longer-lasting than stretch-sensors, have the ability to bear severe conditions and operate within a wide range of temperatures and provide measurements in a wide range of magnetic fields⁹. These sensors also maintain their quality and are generally usable for an unlimited period of time and can perform repeatable operations⁹. Drawbacks to their use include their physical characteristics (e.g., generally involve a solid neodymium magnet) and performance (e.g., interference from external magnetic fields)⁹.

Table 1: Comparison of various wearable technologies for rehabilitation glove (***) Desirable, ** Nominal, * Worst)⁹.

Technology	Accuracy	Performance	Cost	Lifetime
Flex sensor based	***	**	**	***
Accelerometer based	**	***	***	***
Vision based	**	**	*	**
Hall effect based	*	*	**	***
Stretch sensor based	**	**	***	*
Magnetic sensor based	*	**	**	***

In general, all Hall effect based soft force sensors have utilized a solid and rigid neodymium magnet that is limited both by its structure and also because these kinds of sensors tend to have a quick saturation and therefore a limited measurable force range¹⁰. In an investigation designed to identify ferromagnetic options and to minimize the thickness of these materials, Mirzanejad and Agheli developed and described a new soft Hall effect sensor that replaced the typical solid and rigid neodymium magnet with neodymium magnetic powder blended with silicone rubber^{10, 11}. Among their findings, they found that the sensor could measure forces in the range of 0-20 N with a sensitivity of 2.85 mV/N (linear fitting) and a maximum hysteresis error of 12% of output span. They were successful in implanting the sensor into the body of a cylindrical soft pneumatic actuators to measure the axial extending force. Overall, these findings indicate that the use of a ferromagnetic powder such as neodymium incorporated into a soft piece of silicone rubber has significant advantages. First, by removing the solid magnet and using a ferromagnetic powder in a soft silicone the sensor is now softer, without rigid parts, and has a greater potential for use in soft robotic applications. Second, the strong field of neodymium magnets causes the Hall effect sensors to saturate very quickly, which is extremely undesirable especially in thinner sensors where the distance between the sensor and the magnetic part may be very small. Using other formulations such as a magnetic powder,

which has a weaker magnetic field compared to solid magnets, ensures force detection without quick saturation of the sensor^{12, 13}. Overall, these characteristics may result in a ferromagnetic-polymer sensor that has a greater applicability in soft robotic systems and clinical sensing applications.

Sensitivity is a key component in the applicability of a sensor. In a recent investigation of a wireless wide-range pressure sensor, Kou and colleagues (2019) investigated a flexible graphene/PDMS sponge as a dielectric layer sandwiched between the folded surfaces of a flexible printed circuit¹⁴. By adjusting the concentrations of graphene and NH_4HCO_3 concentrations they developed a composite (20% NH_4HCO_3 /2% graphene as the dielectric layer) that exhibited a high sensitivity, a wide operating range, a rapid response time, low detection limit, and good stability, recoverability, and repeatability. They proposed that this composite and wireless pressure sensor has the potential for a wide range of applications including robotics¹⁵ and wearable electronic skins¹⁶⁻¹⁸ and devices¹⁹⁻²¹.

Collaborative Data

The Berkland Laboratory at the University of Kansas has been investigating ferromagnetic compounds in silicone cushions that may be sensed remotely in order to identify those compounds with the highest potential for commercial utilization in a number of technical applications such as wireless sensors. In one of the most recent investigations to date, several of our lab members created 3D printed silicone cushions using NuSil R40 as seen in Figure 1 and then evaluated the magnetic properties of nickel nanorods suspended in the NuSil R40.

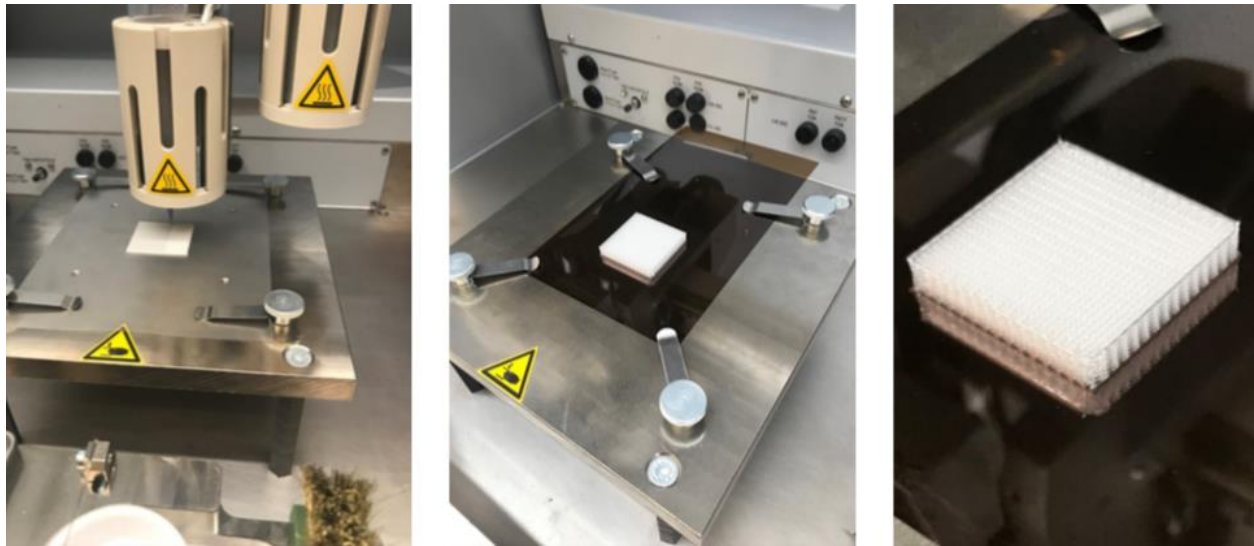


Figure 1: 3D printing of NuSil R40-2181 in an EnvisionTEC 3D-Bioplotter.

In their initial evaluations of 10 weight percent (wt %), 1 wt %, and 0.1 wt % concentrations of nickel nanorods in NuSil R40, they found that the nickel nanorods extruded well in the silicone inks and aligned in the direction of flow (Figure 2). NuSil R40 extrusion tests were also performed using 1 wt % nickel nanorods of varying lengths, specifically categorized as small (1-4 μm), medium (4-8 μm), and large (8-12 μm) (Figure 3).

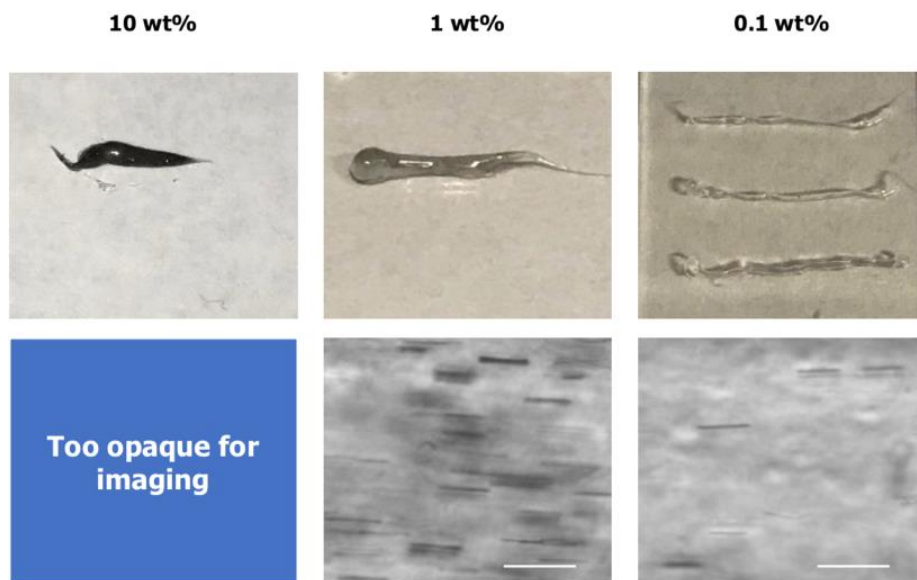


Figure 2: Extrusion tests of nickel nanorods in NuSil R40 at 0.1, 1, and 10 wt %. The scale bars are equal to 20 μm .

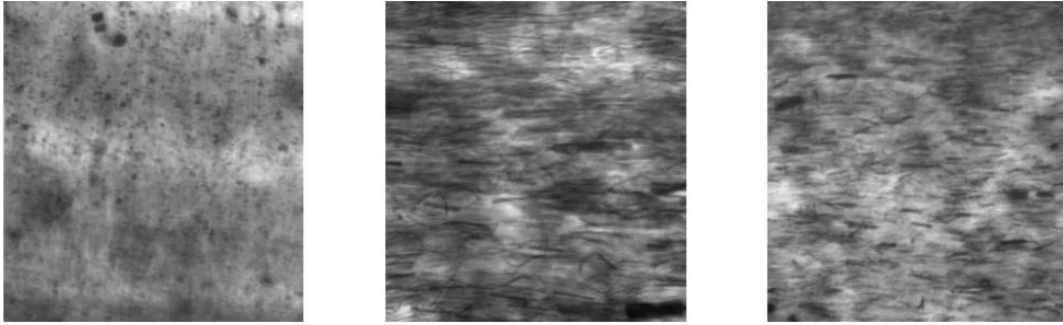


Figure 3: Microscope imaging of 1 wt % (small = 1-4 μm [left], medium = 4-8 μm [middle], and large = 8-12 μm [right]) nickel nanorods in NuSil R40.

Previous work also briefly analyzed the viscoelasticity of medium and large ferromagnetic nickel nanorods at 1 wt % within NuSil R40 using a TA Instruments AR 2000 Rheometer. The viscosity (Figure 4A) as well as the storage and loss moduli (Figure 4B) of the 1 wt % medium and large nickel nanorods in NuSil R40 were relatively similar to that of controls of NuSil R40 with 0 wt % nanorods. Results indicated rheological properties were maintained and additive manufacturing techniques could be conducted when including these magnetic nanorods within polymers.

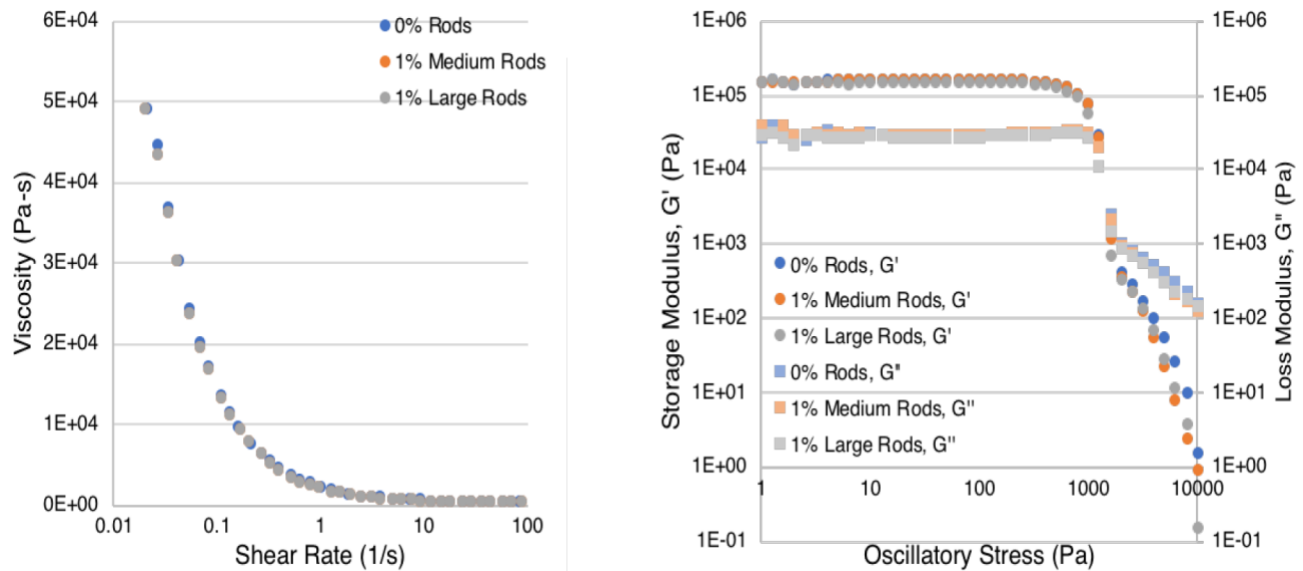


Figure 4: Viscoelasticity of 1 wt % medium and large nickel nanorods within NuSil R40.

The 3D printing process using NuSil R40 with nickel nanorods produced similar silicone cushions across the 0, 0.1, 1, and 10 wt % nickel nanorod concentrations. The silicone cushions could be magnetically manipulated with their fidelity maintained following the curing process. Directional mechanical testing of horizontal nickel nanorods was performed on a TA Instruments RSA3 Dynamic Mechanical Analyzer (DMA) and found a greater compressive modulus (kPa) as the nanorods lengths were increased as depicted in Figure 5A. Compressive strength was also evaluated with 1 wt % of medium vertical nanorods (with vertical being defined as a 40% vertical alignment of nickel nanorods) and found a greater compressive modulus within the vertically rather than the horizontally aligned rods (Figure 5B).

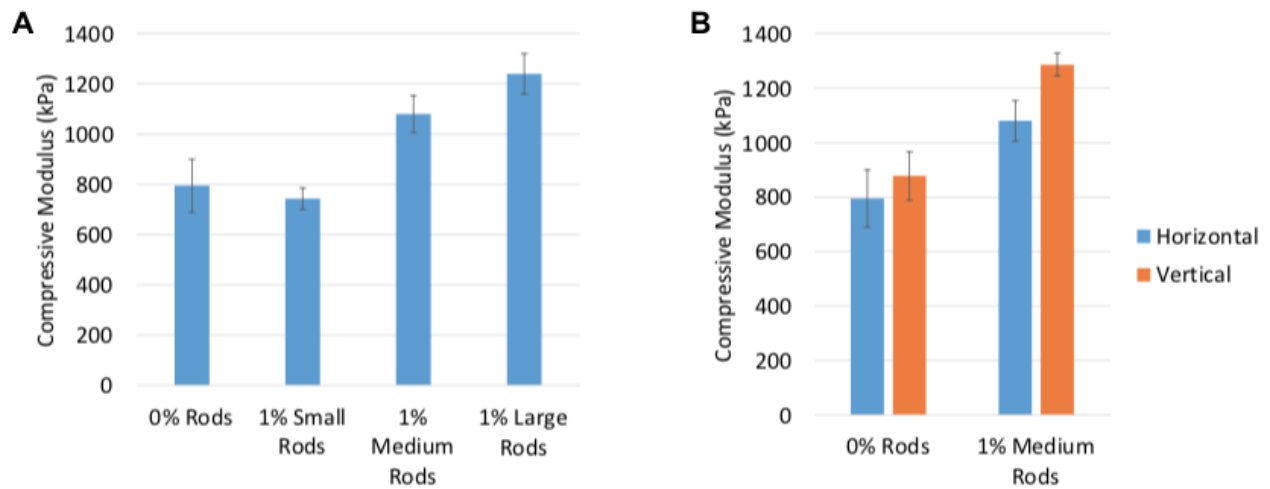


Figure 5: Directional mechanical testing of 1 wt % horizontal and vertically aligned medium (4-8 μm) PDMS-nickel nanorod constructs.

Further evaluations of compression resistance were performed with the implementation of horizontally and vertically aligned nickel nanorods within PDMS at increasing levels of magnetic field strength. An electromagnet was placed directly underneath the samples on the DMA and the baseline compressive modulus of these horizontal and vertically aligned nickel nanorods was evaluated within PDMS when no magnetic field was applied. Then, as illustrated in Figure 6, the application of magnetic energy resulted in no significant change of vertically

aligned nanorods within PDMS. However, PDMS cylinders with horizontally oriented nickel nanorods displayed a near four-fold increase in compression moduli as an increased magnetic field was applied, thus stiffening the PDMS as a function of magnetic field strength.

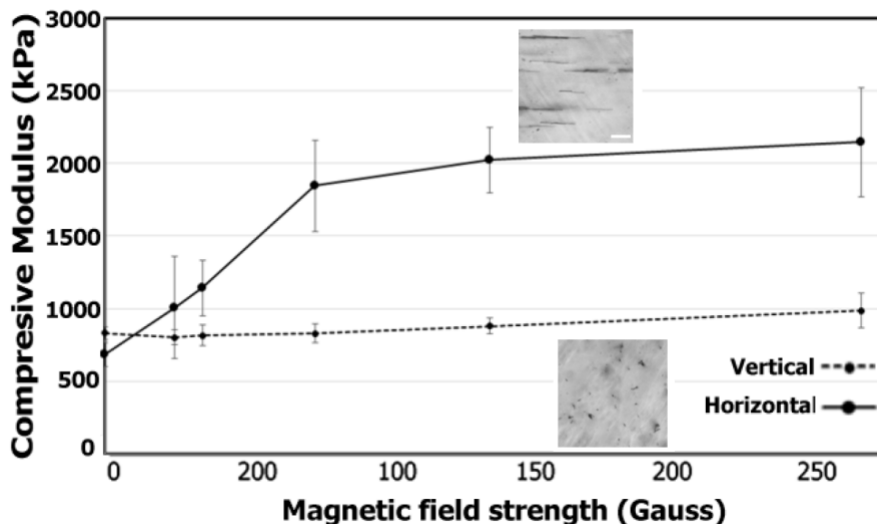


Figure 6: Compressive modulus as a function of magnetic field strength of 1 wt % horizontal and vertically aligned medium (4-8 μm) PDMS-nickel nanorod constructs.

Remote compression sensing was evaluated using a Hall effect sensor placed directly underneath samples on the DMA. PDMS cylinders and NuSil R40 cushions with 1 wt % nickel nanorods were sensed for their magnetic field strength at varying levels of compression force over time (in seconds). As illustrated in Figure 7, increasing the force of compression from 100 g to 600 g (in compression intervals of 100 g) produced an increase in magnetic field strength in both the PDMS cylinders (Figure 7A) and in the NuSil cushions (Figure 7B) with 1 wt % nickel nanorods.

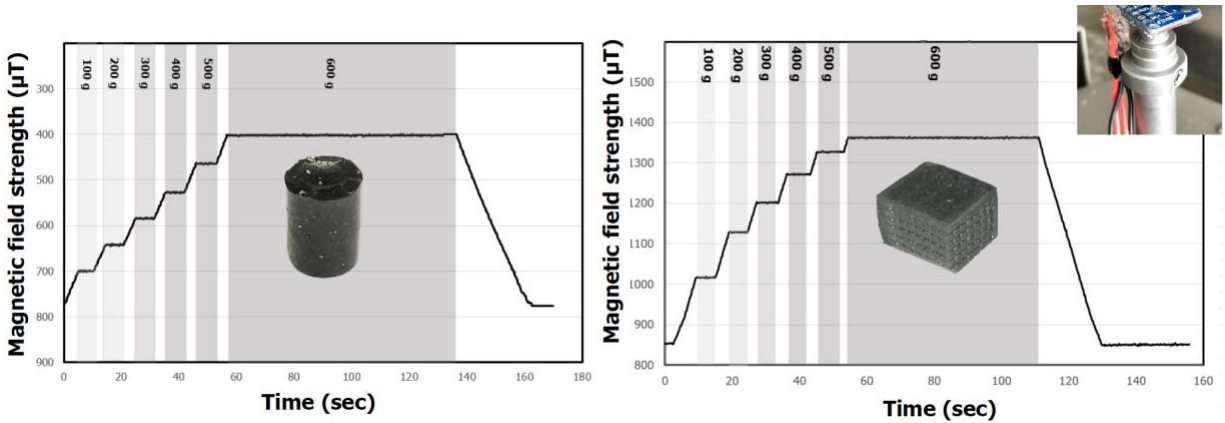


Figure 7: Quantitative sensing of PDMS and NuSil R40 cushions with 1 wt % nickel nanorods.

Findings indicated that the orientation of the nickel nanorods in the composite affected the magnetic field strength. At the same compression intervals, PDMS cylinders with horizontally aligned nickel nanorods displayed a greater increase in magnetic field strength when compared to cylinders with vertically aligned nickel nanorods (Figure 8).

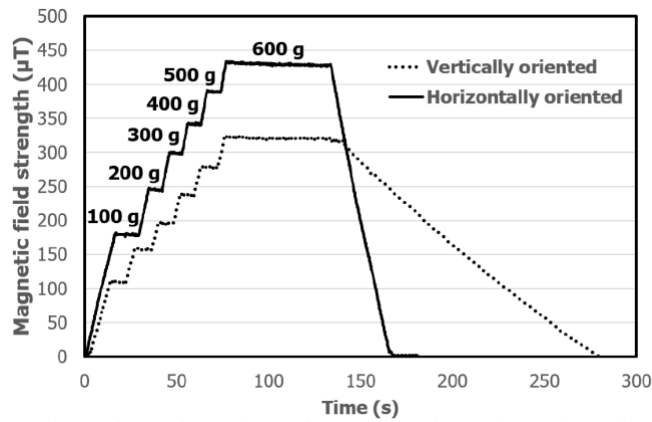


Figure 8: Changes in magnetic field strength in 1 wt % horizontal and vertically aligned PDMS-nickel nanorods constructs at various compression intervals.

Sensing of movement, especially that in three directions, is an important characteristic of the next generation of smart materials. In evaluations of the PDMS-nickel nanorod 1 wt % composite the cylinder movement was sensed in the three directions and displacement of different magnitudes and durations were evident (Figure 9).

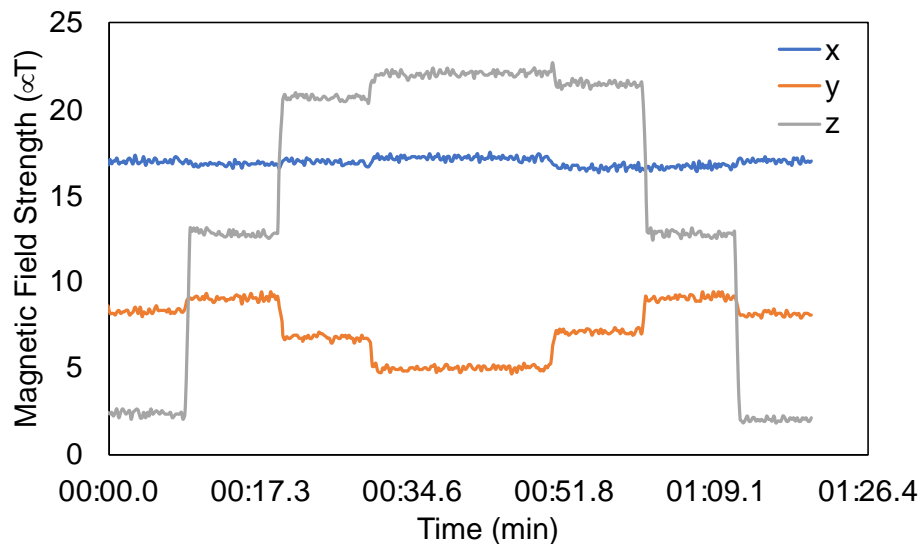


Figure 9: Magnetic field response from the x, y, and z axis of a 1 wt % PDMS-nickel nanorod construct during different magnitudes of displacement.

The results from these investigations by our colleagues were that silicone cushions with a PDMS-nickel nanorod 1 wt % composition displayed electromagnetic-induced stiffness with remote control and that movement in a three-directional fashion was sensed using a remote magnetometer. The findings also suggest that horizontally aligned nickel nanorods display a greater change in magnetic field strength than vertically aligned nanorods.

State of the Art Summary and Objectives

The state of the art in wearable electronic devices and specifically soft materials and sensors has improved dramatically through innovative investigations into materials, capacity to detect compression, sensitivity, measurements means, and accuracy. Several have reported that soft materials can be 3D printed and that the incorporation of magnetic nanoparticles (e.g., magnetic powders rather than solid magnets) have the ability to detect compression events on a more sensitive level with no loss in accuracy. Our collaborative efforts have shown that the physical properties of soft materials change with the incorporation of magnetic particles. These materials also display a change in their magnetic field response when compressed. Specifically,

when 600 g of force was applied to PDMS with 1 wt % nickel nanorods, there was a 350 μ T increase in magnetic field strength. In addition, as many have noted, there are limitations in accuracy and performance of Hall effect sensors. Based on these shortcomings and prior investigations, the research presented here was designed to: 1) test additional magnetic fillers, 2) to investigate the dependence of magnetic filler concentration on the sensitivity of detection, and 3) to evaluate magnetic fillers in additional types of soft materials. Ideally, these investigations will lead to the identification of new materials that when combined with a Hall effect sensor, will improve its accuracy and sensitivity.

Chapter 2: Compression Testing of Ferromagnetic Particles Within Soft Materials

Introduction

The rapid advancements in soft materials has spurred the development of smart sensing devices including those that may be implantable into various textiles or other sensing applications. These smart materials are comprised of magnetic particles to enable detection of material movement or even control of movement via external magnetic fields. Such soft materials can be applied in a number of fields which include soft robotics^{22, 23}, biomechanics^{24, 25}, as well as and biomedical^{26, 27} and biotechnology²⁸ applications such as drug delivery²⁹, imaging^{30, 31}, monitoring^{14, 32}, and invasive surgery^{33, 34} devices. However, there is still a need to improve the accuracy and performance of these soft sensors.

Until recently, Hall effect sensors generally utilized a solid and rigid neodymium magnet embedded within silicone or other soft materials. These were limited both by its structure but also because these kinds of sensors tend to reach saturation quickly and therefore offer a limited range of measurement¹⁰. The need to improve these sensors lead to an investigation designed to identify a way to replace rigid neodymium magnets with a neodymium magnetic powder that could then be blended with silicone and cured¹¹. This technique reduced the overall thickness and resulted in the development of a sensor with a softer structure.

Numerous synthetic polymers and soft materials are on the market, however the need to improve materials and performance of soft sensors is fundamental³⁵. Soft materials need to be durable as to not break from repeated amounts of compression and have sufficient recovery to sustain their shape. They also need to maintain the ideal rheological properties prior to curing if additive manufacturing techniques of these soft sensors is to be explored^{36, 37}. Silicones have become favorable due to their low cost as well as their ability to be printed through direct ink

writing (DIW)³⁸. They also express the ability to change physical properties due to varying molecular weight, chemistry, and weight-to-weight (w/w) ratios of the base polymer to crosslinker^{39, 40}.

Magnetic particles used as fillers for soft materials would need to possess the ability to emit a large magnetic field and retain their magnetic moment. In addition, they would have a high remnant magnetization and have a large coercivity to avoid demagnetization. Before chemical synthesis of ferromagnets, this was considered an anomaly because materials that have a large coercivity tend to have low remnant magnetization and those with a high remnant magnetization tend to have a low coercivity³⁰. Therefore, we explored synthetic ferromagnetic fillers such as cobalt, iron, nickel, and their common alloys because of their abilities to retain permanent magnetism. We also considered the particle shape and sizes of these magnetic fillers in an effort to avoid affecting the bulk properties of the soft materials. This is especially vital in situations where the function of the soft material must be maintained.

The current state of the art in magneto sensing has revealed several limitations with regards to both magnetic particle performances as well as materials. Specifically, the key components are to improve upon sensitivity, accuracy, and performance^{9, 10}. This study sought to advance previous magnetic sensing research and our own collaborative data to improve current force sensors, specifically the limitations in sensitivity and accuracy. We designed these investigations to identify and test six ferromagnetic fillers incorporated within soft sensors. Our main objective was to analyze the magnetic concentration dependence on the ability to detect compression events and their magnetic field response generated during these compression events. Next, we wanted to assess a particular ferromagnetic filler with a viable magnetic field

response to identify other possible soft materials and composites with potential in future sensing applications.

Materials & Methods

Nickel Nanorod Synthesis

Ferromagnetic nickel nanorods utilized in the testing were synthesized by electrodeposition of nickel into nanoporous alumina templates⁴¹. To perform the process supplies were acquired as follows: Whatman™ Anodisc™ Filter Membranes of 0.02 μm pore size were obtained from Fisher Scientific (Hampton, NH, USA); gallium–indium eutectic, nickel(II) chloride hexahydrate, nickel(II) sulfate hexahydrate and boric acid used in the electrolyte solution were obtained from Sigma Aldrich (St. Louis, MO, USA); and nickel wire of 1.0 mm diameter 99.5 % metals basis was purchased from VWR (Radnor, PA, USA). Previous work demonstrated that varying the deposition time produced nanorods of assorted lengths: 10-20 minutes produced small (1-4 μm), 20-30 minutes produced medium (4-8 μm), and 40-50 minutes produced large (8-12 μm) nanorods. All nickel nanorods synthesized and produced for this work utilized a deposition time of 45 minutes.

Remaining Magnetic Materials

Aside from the nickel nanorods being produced in lab, the five remaining ferromagnetic materials were obtained from and used as received from outside suppliers. Carbonyl iron microspheres, cobalt nanowires, and iron(II,III) oxide (iron oxide) nanopowder were all acquired from Sigma Aldrich (St. Louis, MO, USA). The iron oxide contains a 97 % trace metal basis. Magnetite powder and neodymium iron boron (neodymium) powder were purchased from Advanced Reade Materials (East Providence, RI, USA) and Nanoshel (Wilmington, DE, USA), respectively. The purity of the neodymium powder is 95-96 % and comprised of 29-32 %

neodymium, 64.2-68.5 % iron, 1.0-1.2 % boron, and 0.5-1.0 % niobium. Physical properties of the magnetic materials were provided in their technical data sheets by their respective suppliers and are summarized in Table 2.

Table 2: Physical properties of ferromagnetic materials.

Magnetic Material	Diameter/Average Particle Size	Length (μm)	Density (g/cm^3)
Carbonyl Iron	1 μm	-	7.86
Cobalt	200-300 nm	100-200	8.90
Iron Oxide	50-100 nm	-	4.8-5.1
Magnetite	5 μm	-	5.1
Nickel	100-200 nm	8-12	-
Neodymium	50-60 μm	-	7.5

Characterization

Each magnetic material was imaged using a light microscope and their particle sizes and lengths were verified using ImageJ. Previous work utilized transmission electron microscopy (TEM) to measure the diameters of the synthesized nickel nanorods and to examine their nanoscale features.

Soft Materials

Three silicones and a two-part polyurethane were also purchased from outside suppliers to be utilized as soft materials. Dow Sylgard™ 184 silicone elastomer base and curing agent was acquired from Dow Chemical Company (Pevely, MO, USA). It is a two-part system comprised of a polymeric base and a curing agent that when combined, the curing agent crosslinks with the polymeric matrix to form PDMS. Two additional vinyl terminated polydimethylsiloxanes (DMS-V21 and DMS-V33) and platinum-cyclovinylnmethyl-siloxane complex; 2% pt in cyclomethylvinylsiloxanes (platinum catalyst) were purchased from Gelest (Morrisville, PA, USA). The Sylgard 184 curing agent was used as the crosslinker and the platinum catalyst was also used to help cure these two siloxanes. The supplier recommends using a 10:1 w/w ratio of

base to curing agent for PDMS, however, a 15:1 w/w of base to curing agent was used for all three silicones. A two-part polyurethane (BJB) was also obtained from BJB Enterprises (Tustin, CA, USA). The polyurethane mixture needs equal parts (1:1 w/w) of each component to cure. Table 3 lists the respective densities (kg/m³) and viscosities (cSt) of the soft materials used as provided by their respective suppliers' technical data sheets.

Table 3: Physical properties of uncured soft materials.

Soft Material	Density (kg/m³)	Viscosity (cSt)
BJB	1,050	1,100
DMS-V21 Base	970	100
DMS-V33 Base	970	3,500
PDMS Base	1,110	5,000
Sylgard 184 Curing Agent	1030	110

Preparation of Samples

The dry powder of all six ferromagnetic materials were incorporated into PDMS at varying concentrations of 0.01, 0.1, and 1 weight percent (wt %). The powder was first weighed before adding the PDMS base and curing agent at a 15:1 w/w ratio. The samples were hand mixed aggressively using glass stirring rods and then centrifuged at 500 min⁻¹ to eliminate any air bubbles without separating components. Uncured samples were then mixed lightly again before being filled into 96 well-flat bottom plates (Corning Incorporated; Corning, NY, USA) and placed in a vacuum chamber for 20 to 30 minutes before curing to remove any additional air bubbles (Figure 10A). Following this process, the samples were then placed in an oven at 70 °C to decrease curing time from 24-48 hrs at room temperature to just 2-3 hours. To produce horizontally-oriented dipoles of ferromagnetic particles within the PDMS, samples were prepared by applying a 15 gauss magnetic field (~ 0.1 T) with an electromagnet mounted perpendicularly to the samples during curing (Figure 10B).

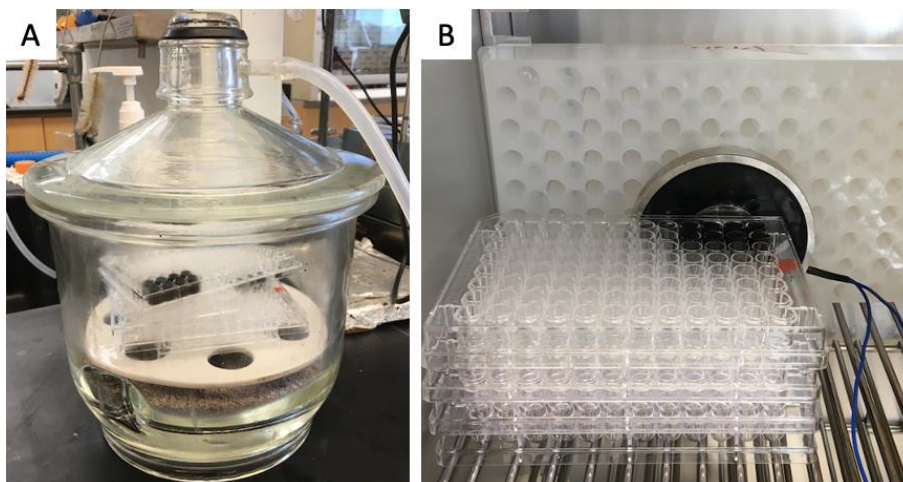


Figure 10: A) Vacuum chamber for removing air bubbles prior to placing samples in oven. B) Samples with electromagnet mounted perpendicularly inside curing oven set at 70 °C.

After curing was completed, the well plates were broken down and samples were removed from individual wells using ethanol. Due to the silicones surface tension within the individual wells, menisci had formed and were removed by slicing the top part of the cylindrical constructs to bring their height down from about 10.65 mm to approximately 7.50 mm. Samples were also brought down to this height to help prevent shear stress during testing. The samples each had a diameter of 6.5 mm.

Iron oxide nanopowder was also mixed with the remaining silicones, DMS-V21 and DMS-V33, as well as the BJB polyurethane at 1 wt %. The iron oxide was utilized as the control within these soft materials due to its abundance and inexpensive cost as well as its magnetic field strength displayed in preliminary studies. The DMS-V21 and DMS-V33 were prepared in similar fashion to the PDMS as each was used at a 15:1 w/w ratio of base to curing agent with an additional 0.01 volume % of platinum catalyst. with the iron oxide following the weighing, centrifuging, vacuum chamber, and oven. The BJB polyurethane cures within 30 minutes at room temperature so once it was mixed and centrifuged with iron oxide at 1 wt %, it was left to cure at room temperature.

Compression Testing and Sensing

A MLX90393 triple-axis magnetometer purchased from Adafruit Industries (New York City, NY, USA) was wired to an Arduino Mega 2560 microcontroller to communicate via I2C, and the magnetometer board was then mounted using double sided tape onto the bottom geometry platform of the Electroforce 5500 (TA Instruments, Eden Prairie, MN, USA). Cylindrical constructs were subsequently placed above the magnetometer sensor and the ElectroForce 5500's axial mover was lowered until contact was made with the top side of the sample (Figure 11A). The ElectroForce was utilized to exert increasing increments (i.e., 0-600 g in increments of 200 g over 10 seconds) of compressive force on the samples (Figure 11B and C) for the first half of the experiment and then release those same incremental amounts of force until zero force is applied at the end. Each compressive force was held for 10 seconds. Magnetic field strength data from all three axes were collected from the output of the Arduino IDE software while the samples were compressed by the ElectroForce 5500. Magnetic field strength readings from the magnetometer were plotted against time alongside the applied force. Remote sensing of compression events was successfully achieved; both duration and magnitude of compressive forces were detectable based on the change in magnetic field strength. This procedure was also conducted with blank PDMS, DMS-V21, DMS-V33, and BJB constructs without the ferromagnetic materials to establish a baseline reading of magnetic field strength and possible background interference.

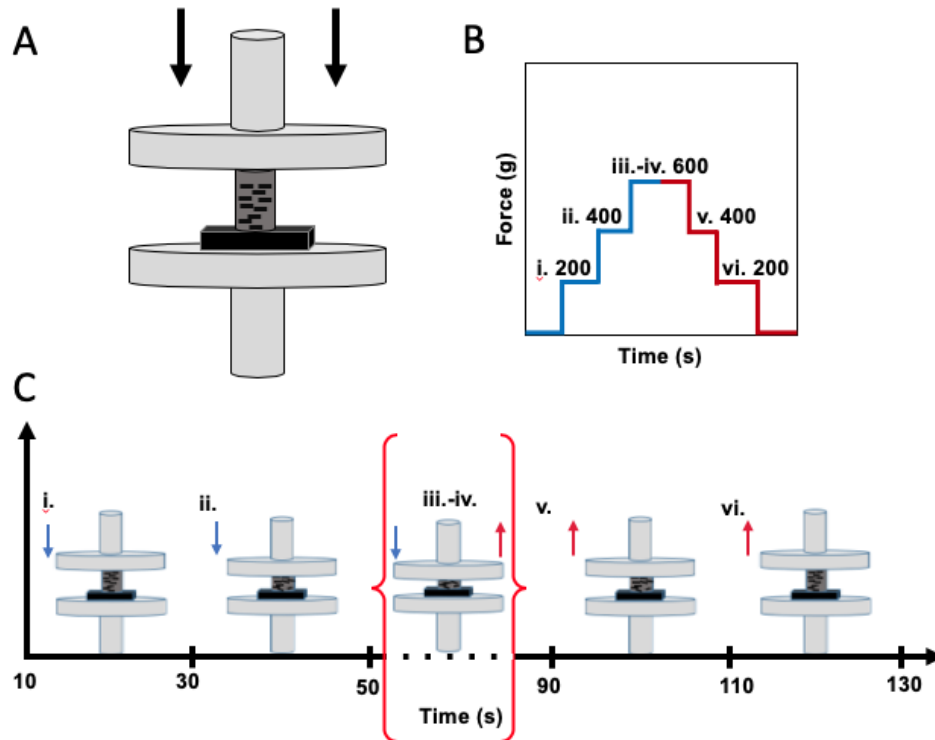


Figure 11: Experimental setup of compression testing. A) Cylindrical sample is placed on top of magnetometer and top geometry of ElectroForce 5500 is lowered to sample height until contact is made. B) Theoretical graph of force (g) versus time (s) showing the incremental steps of 200 g of force applied at 20 g/s for steps i, ii, and iii, and the removal of 200 g of force applied during steps iv, v, and vi. C) Theoretical figure of a cylinder being compressed or recovered during each incremental step of applied force over the course of 140 s.

Prior to using the ElectroForce 5500, preliminary studies were also performed using a similar technique as seen in Figure 11. However, rather than measuring the magnetic field response based on applied force, the magnetic field strength was measured against displacement. A NEMA-23 two-phase stepper motor was modified with platforms to add compression geometry onto the linear actuator. This custom built stepper motor seen in Figure 12A was then used to apply increasing increments (i.e., 0-2.25 mm in increments of 0.75 mm) of displacement on the samples seen similarly in Figure 11B and C. A LSM303 triple-axis accelerometer and magnetometer purchased from Adafruit Industries was mounted onto the bottom platform geometry using double sided tape. The cylindrical construct was then placed on top of the

magnetometer before the top geometry platform (mounted to linear actuator) was lowered until contact with the top side of the sample was made (Figure 12B). Two separate Arduino Mega 2560 microcontrollers were then used to communicate with the magnetometer and the stepper motor via an A4988 stepper motor driver.

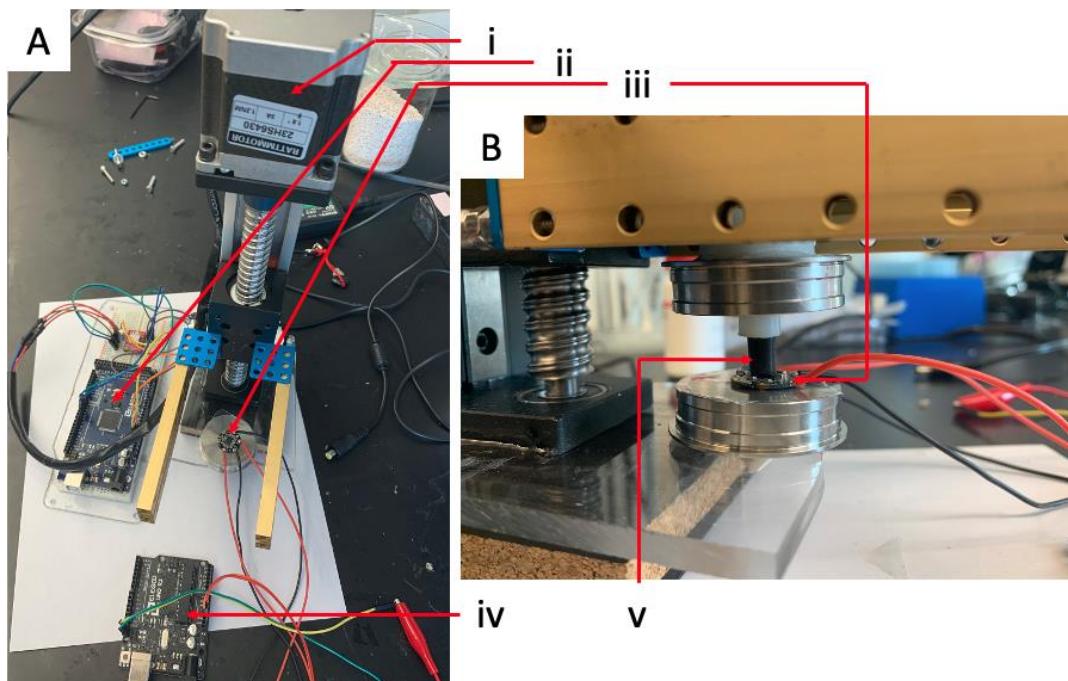


Figure 12: A) Custom built stepper motor to perform preliminary studies B) Compression geometry of stepper motor i) NEMA-23 2 phase stepper motor ii) Motor controller with A4988 stepper motor driver and iii) LSM303 triple-axis accelerometer and magnetometer iv) Sensor controller v) Cylindrical sample to be compressed.

Statistical Analysis

Statistical analyses were performed using SAS statistical software. One-way analysis of variance was used to determine whether statistically significant differences were present between means of various ferromagnetic materials. Two-way ANOVA was used for experiments with iron oxide embedded within various soft materials. The Dunnett method was used for post-hoc comparisons against the blank PDMS controls at a 95 % ($\alpha = 0.05$) family-wise confidence level. Statistical significance was considered when the determined p-value was less than 0.05 ($p < 0.05$).

Results & Discussion

Cylindrical constructs consisted of the six different magnetic fillers mixed with PDMS at varying concentration levels of 0.01, 0.1, and 1 wt % to determine the sensitivity for analyzing magnetic field strength (μT). These six ferromagnetic particles consisted of nickel nanorods, carbonyl iron microspheres, cobalt nanowires, iron oxide nanopowder, magnetite nanopowder, and neodymium iron boron powder. Iron oxide was also mixed with DMS-V21, DMS-V33, and BJB at 1 wt %. Blank cylinders of BJB, DMS-V21, DMS-V33, and PDMS with no magnetic nanoparticles served as controls to provide a baseline reading on the magnetometer and identify any possible background interference.

Before these cylindrical constructs were produced, the average particle sizes of these six ferromagnetic materials were verified under a 20x light microscope. Figure 13A displays the nickel nanorods and the carbonyl iron, cobalt, iron oxide, magnetite, and neodymium particles can be seen in Figure 13B, C, D, E, and F, respectively.

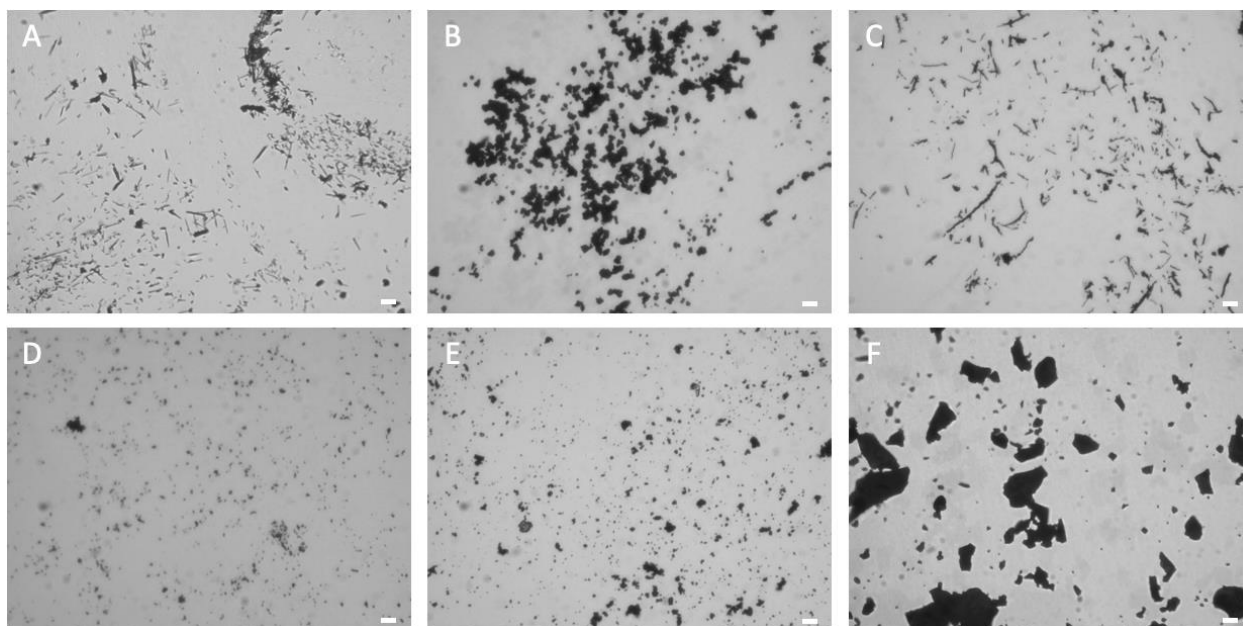


Figure 13: A) Nickel nanorods, B) carbonyl iron microspheres, C) cobalt nanowires D) iron(II,III) oxide (FeO and Fe_2O_3) nanopowder, E) magnetite (Fe_3O_4) powder F) neodymium iron boron powder. The scale bars are equal to 10 μm .

Samples were made in batches and three constructs of each particle were selected for testing ($n=3$). Overall, 72 samples were tested and the ensuing results of the magnetic field strength and displacement (mm) were averaged. Criteria for testing included: 1) no visible air bubbles although this standard became harder to implement in samples at 1 wt % due to their opaqueness as well as within BJB since it cured so quickly and 2) most perpendicular top sides after samples were sliced down from 10.65 mm to 7.5 mm in height to help minimize possible shear stress. It should also be noted that during preliminary trials, only one ($n=1$) of every sample made from nickel, carbonyl iron, iron oxide, and magnetite at 0.01, 0.1, and 1 wt % as well as cobalt at 0.01 and 0.1 wt % within PDMS were tested.

Cylindrical constructs of every magnetic material at 0.01, 0.1, and 1 wt % within PDMS was photographed to show how each cured sample appeared after being cured, removed from well plates and sliced down from about 10.65 mm to approximately 7.50 mm (Figure 14).

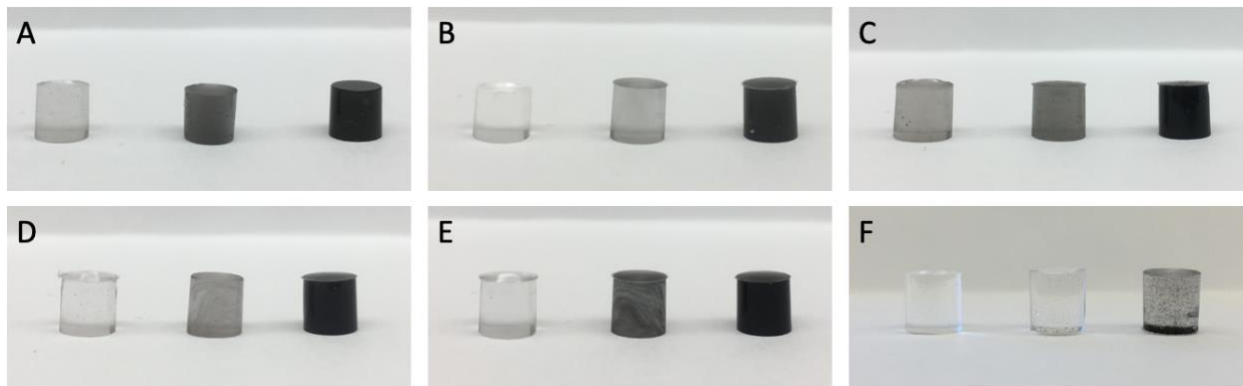


Figure 14: All six ferromagnetic materials at 0.01 wt % (Left), 0.1 wt % (Middle), and 1 wt % (Right) within PDMS. A) Nickel, B) carbonyl iron C) cobalt D) iron oxide, E) magnetite, and F) neodymium.

Figure 15A displays the blank samples of BJB, DMS-V21, DMS-V33, and PDMS with no magnetic filler while Figure 15B presents each of these soft materials with 1 wt % iron oxide. The blank DMS -V33 sample appeared different from the rest of the blanks due to the platinum catalyst that was added. DMS-V21 also includes a platinum catalyst but did not display the darker coloring.

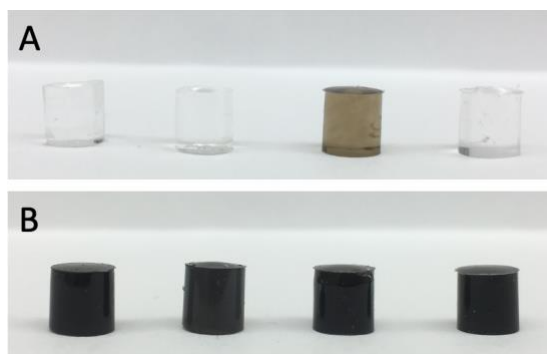


Figure 15: A) Blank samples of 2-part polyurethane (Left), DMS-V21 (Middle-Left), DMS-V33 (Middle-Right), and PDMS (Right). B) Samples each containing 1 wt % iron oxide.

The magnetic field response on the z-axis of each sample was plotted against time along with the change in applied force against time to detail the dependence of the magnetic field response based on force. Figure 16 showcases a typical graph of the magnetic field strength and force plotted against time for a sample of nickel at 1 wt %. The data was normalized to display

the magnetic field response, which was about $1.5 \pm 1.5 \mu\text{T}$ when $0 + 10 \text{ g}$ of force was applied. As the force increased to $200 \pm 10 \text{ g}$, the magnetic field strength increased. When the force was held at a certain point, the magnetic field strength would hold as well. Then, as force was unloaded incrementally, the magnetic field strength of the sample would adjust back to a similar response as when the same force was applied in the first half of the test. This is evident in Figure 16 when the sample is held at $400 \pm 10 \text{ g}$ of force from 40-50 s and displays a magnetic field response of $10.7 \pm 1.5 \mu\text{T}$. Then as the force is increased to $600 \pm 10 \text{ g}$ and reduced back to $400 \pm 10 \text{ g}$ at 90-100 s, the sample exhibits a magnetic field response of about $11.6 \pm 1.5 \mu\text{T}$.

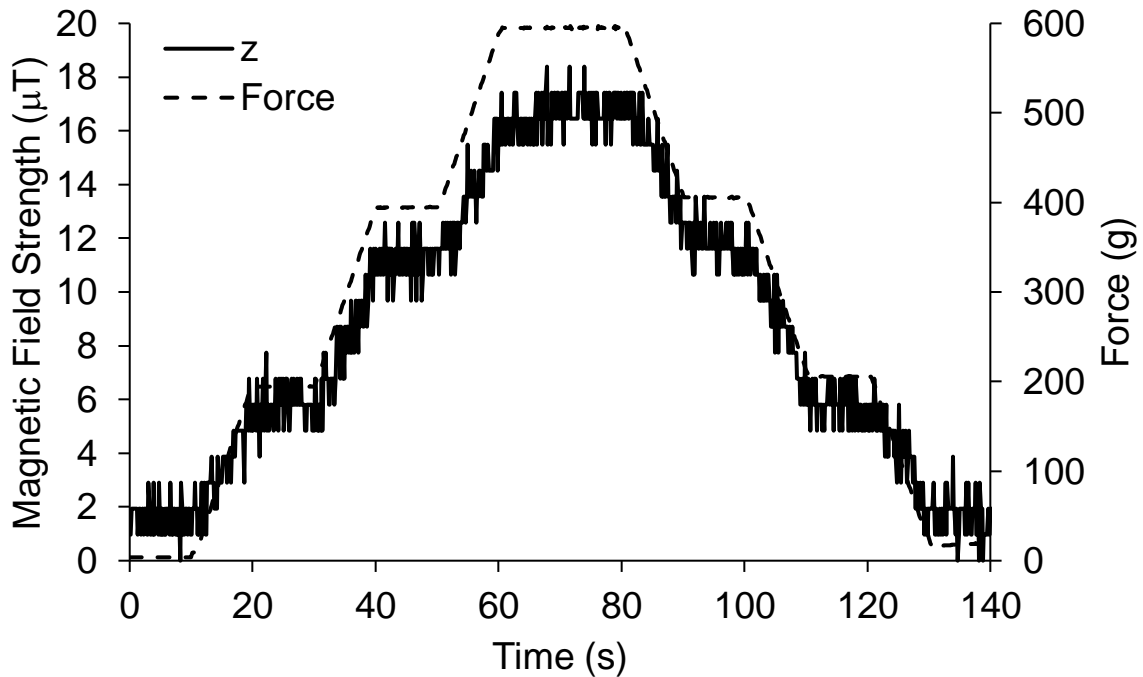


Figure 16: Magnetic field strength (displayed from the z-axis) and the force versus time of a 1 wt % sample of nickel.

Figure 17 outlines the varying ferromagnetic fillers in increasing order of magnetic field strength when 0, 200, 400, and 600 g of force was applied. Neodymium provided the greatest response in magnetic field strength during compression. At 1 wt % and with 600 g of applied force, neodymium exhibited a magnetic field response of $35 \mu\text{T}$. Even with only 200 g of force

applied by the ElectroForce, the neodymium cylinders still provided a magnetic field response (16 μT) equivalent as the next strongest material, nickel, at their maximum force of 600 g. While the nickel was expected to provide a strong magnetic field response, the cobalt was originally hypothesized to produce an even stronger response. However, the cobalt may have displayed a limited magnetic response due to aggregation of the nanowires observed in the cylinders. The blank PDMS control sample provided a baseline reading of about 1.7 μT of background interference on the magnetometer at 0 g of force and about 2.3 μT at about 600 g of force. This could potentially be due to the top geometry and the axial mover interfering with the magnetometer as it approached the magnetometer during compression steps. The iron oxide and magnetite displayed a magnetic field response of about 5 and 4 μT , respectively, at 600 g of force. Meanwhile, the carbonyl iron did not display a magnetic field response strong enough for us to be confident of detection as its maximum response was about 2.5 μT at 600 g of force. Although we were able to observe these changes in the magnetic response with various materials within PDMS, a statistical difference was only observed within nickel and neodymium compared to the blank PDMS ($p < 0.0001$).

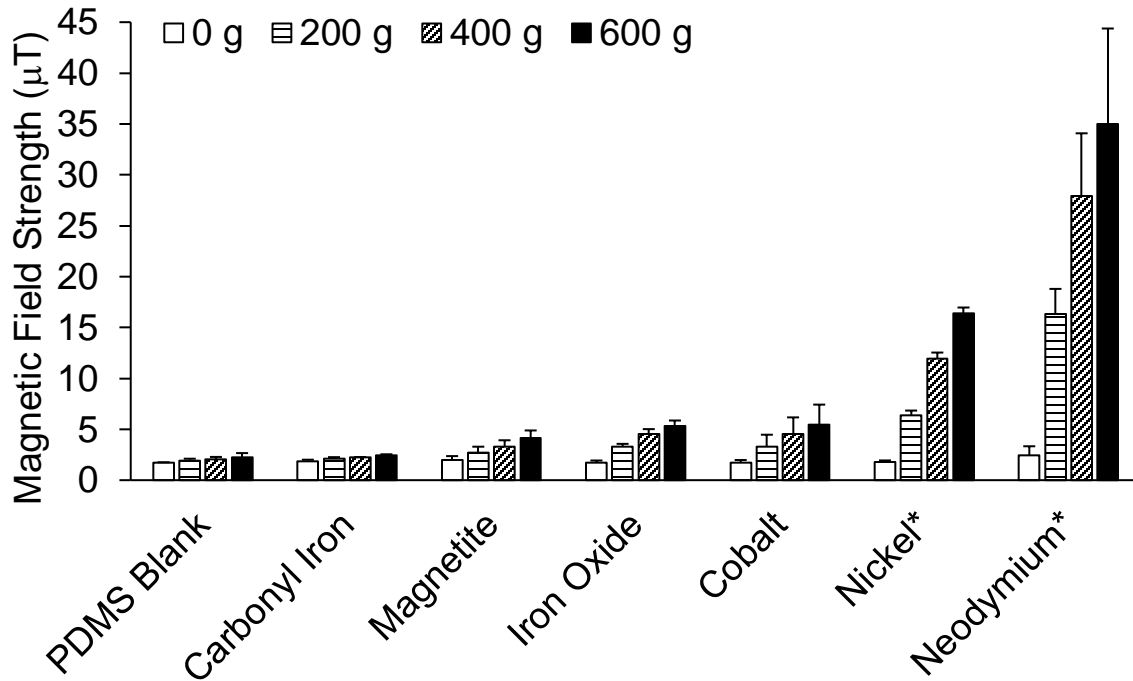


Figure 17: Magnetic field strength from all six magnetic fillers at 1 wt % during 0, 200, 400, and 600 g of force. * denotes statistical difference from PDMS at 600 g of force ($p < 0.0001$).

The ElectroForce was also used to determine the displacement of the samples by measuring the displacement of the axial mover from its starting position to each step of compression. The main motive for quantifying displacement was to identify a similarity between preliminary results performed on the stepper motor compared to the results from the ElectroForce. Figure 18 provides the displacement at of the same 1 wt % nickel sample seen in Figure 16. During 600 ± 10 g of force at 60-80 s, the sample provided a response of about 16.5 ± 1.5 μ T as it was being displaced about 1.83 ± 0.02 mm.

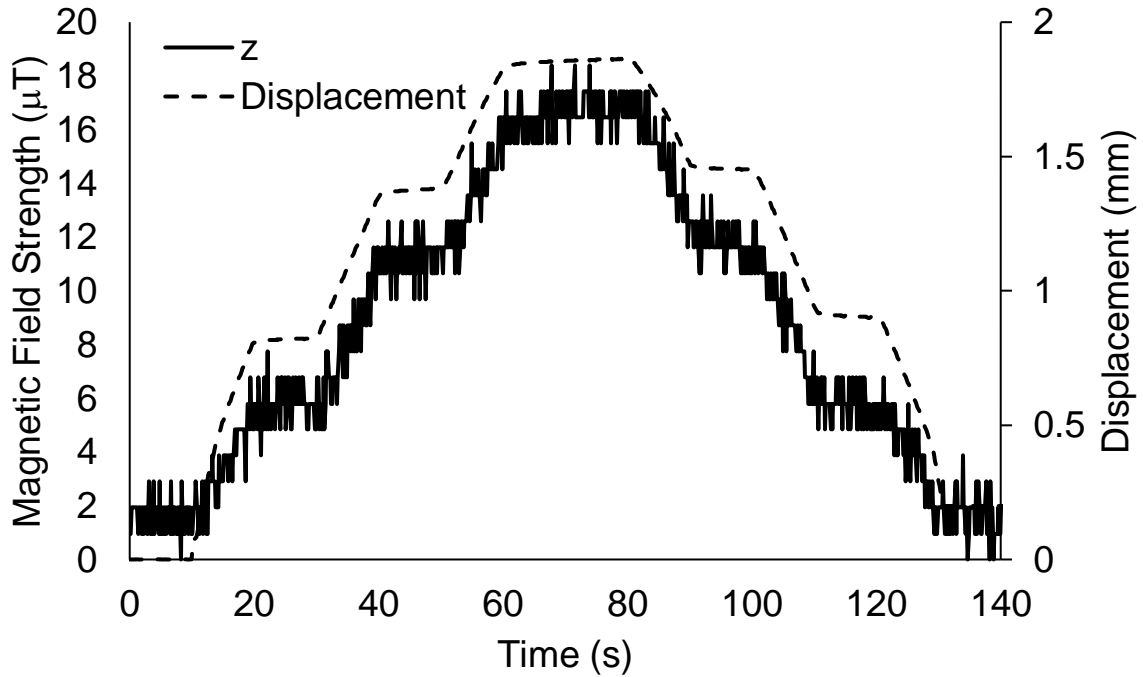


Figure 18: Magnetic field strength (displayed from the z axis) and the displacement versus time of the same 1 wt % sample of nickel depicted in Figure 16.

The average displacements of the three samples tested for each material at 1 wt % during each step of compression can be seen in Figure 19. Although we originally hypothesized each magnetic filler material would have increased the compressive modulus of PDMS, we can see that cobalt, nickel, and neodymium were all displaced an average of 1.82, 1.78, and 1.84 mm, respectively compared to the blank PDMS samples only being displaced 1.62 mm at 600 g of force. Alternatively, carbonyl iron, magnetite, and iron oxide all displayed a higher compressive strength with a lower average displacement of 1.14, 1.44, and 1.46 mm, respectively.

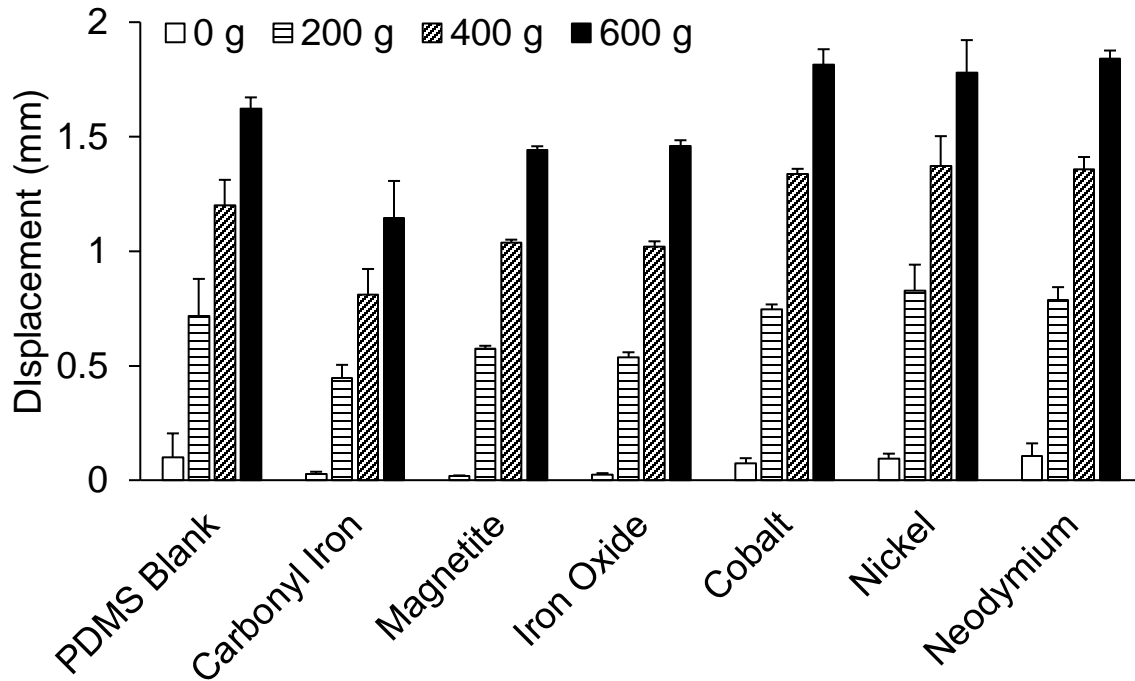


Figure 19: Displacement of all six magnetic fillers at 1 wt % during 0, 200, 400, and 600 g of force.

Returning to the 1 wt % nickel sample seen in Figure 18, Figure 20 provides the actual displacement as a function of force and display a near linear relationship. The compression and decompression cycles are very similar, yet distinct due to the recovery of the constructs. After the force versus displacement curves were plotted for every sample at every wt %, the correlation was used to determine the amount of force applied from the stepper motor at each step of displacement. Figure 21 displays the compressive force vs displacement for one sample of each magnetic material at 1 wt % within PDMS. With this information, a relationship between displacement and magnetic field strength could be modelled in future investigations.

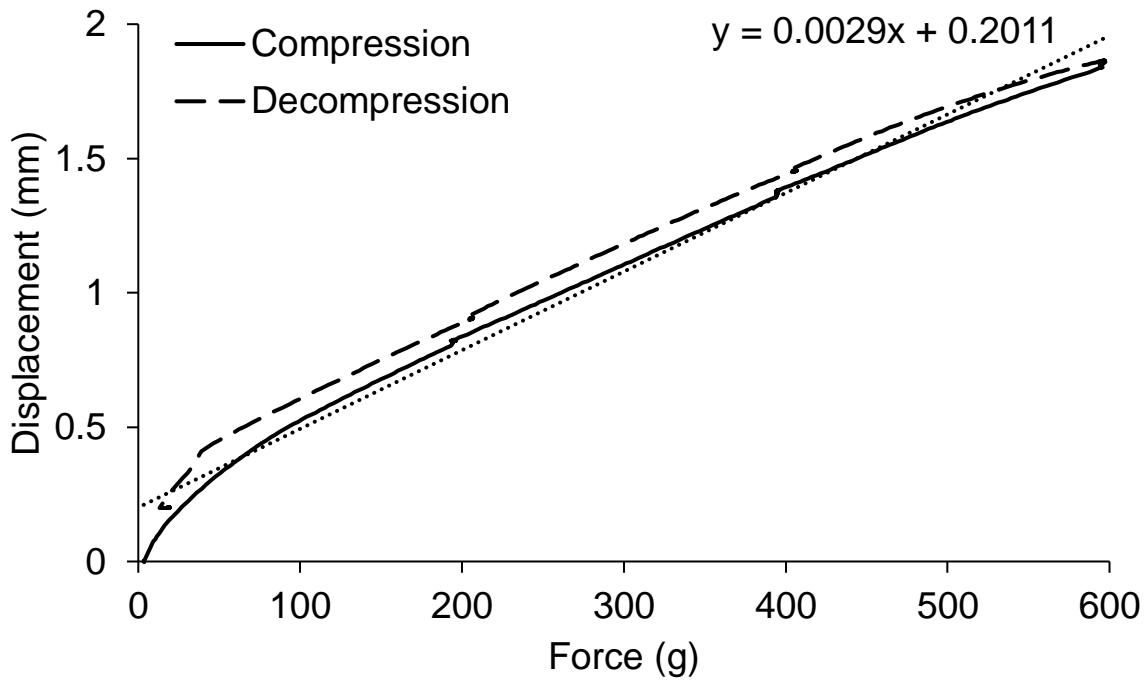


Figure 20: Displacement as a function of force of the same 1 wt % nickel sample seen in Figure 16.

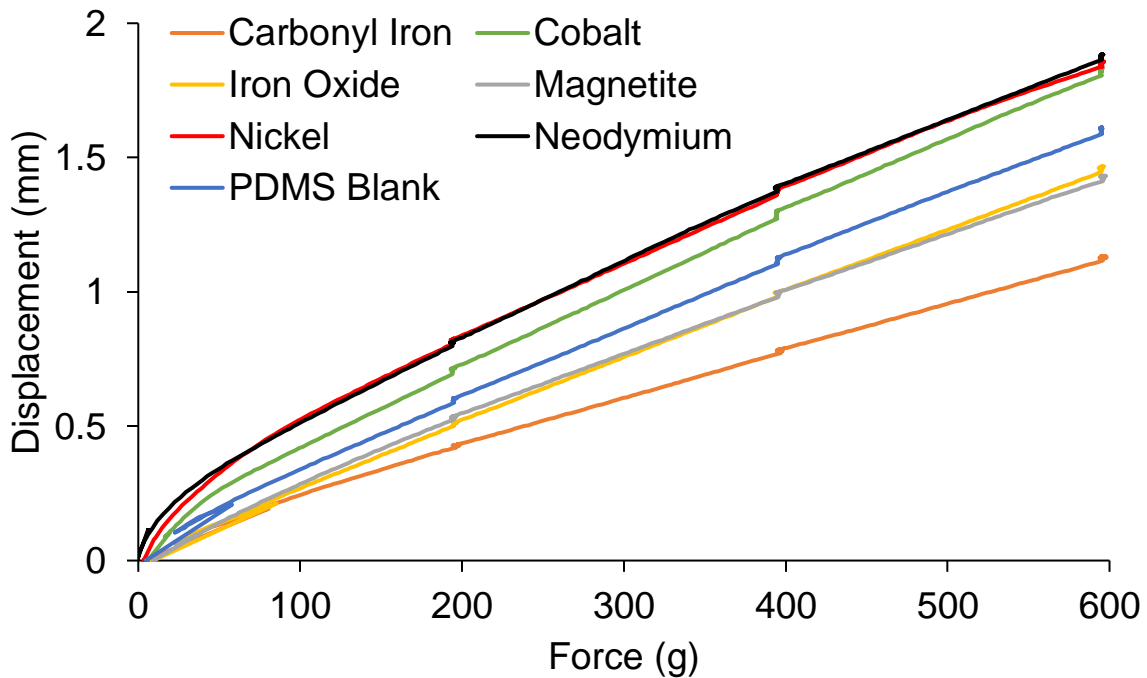


Figure 21: Displacement as a function of force for one sample (n=1) of each magnetic material at 1 wt % within PDMS. Only the compression cycles are displayed here.

When implementing these soft sensors in other applications, we would like to correlate the force and displacement as a function of the magnetic field strength generated during the unknown amount of force and displacement applied. Figure 22 depicts the relationship between displacement and magnetic field response. For example, with neodymium powder incorporated into PDMS at 1 wt %, if the sensor displayed a response of about 30 μT , we could determine the sensor was displaced about 1.4 mm. We can also determine that about 400 g of force was applied during that response when using that information and referring back to Figure 21.

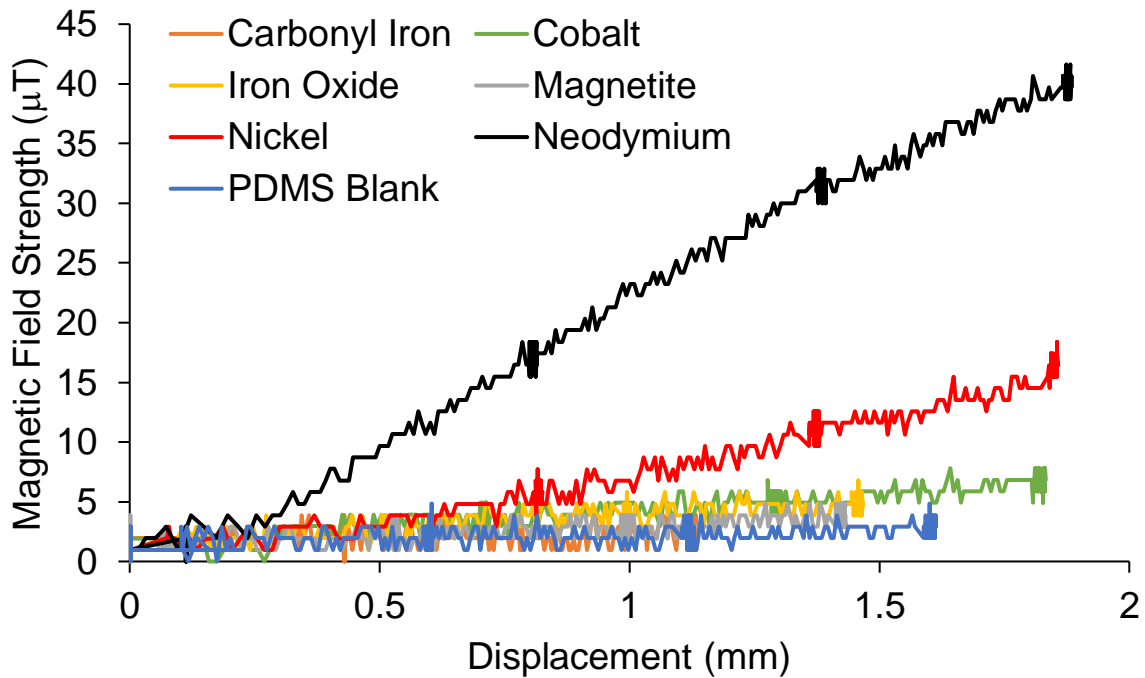


Figure 22: Magnetic field strength as a function of displacement for one sample ($n=1$) of each magnetic material at 1 wt % within PDMS. Only the compression cycles are displayed here.

Figure 23 displays the magnetic field strength produced from the z-axis of a 1 wt % nickel sample originally tested during the preliminary studies on the stepper motor. The sample produced an average magnetic field response of 11.0, 19.3, and 20.2 μT at 0.75, 1.5, and 2.25 mm of displacement, respectively. Using the linear equation in Figure 20 as well as the linear relationships produced from the other two 1 wt % nickel samples, we were able to determine

approximately how much force was applied at each step. At 0.75 mm of displacement, roughly 190 g of force was applied while about 450 g and 700 g of force were applied at 1.5 mm and 2.25 mm steps of displacement, respectively.

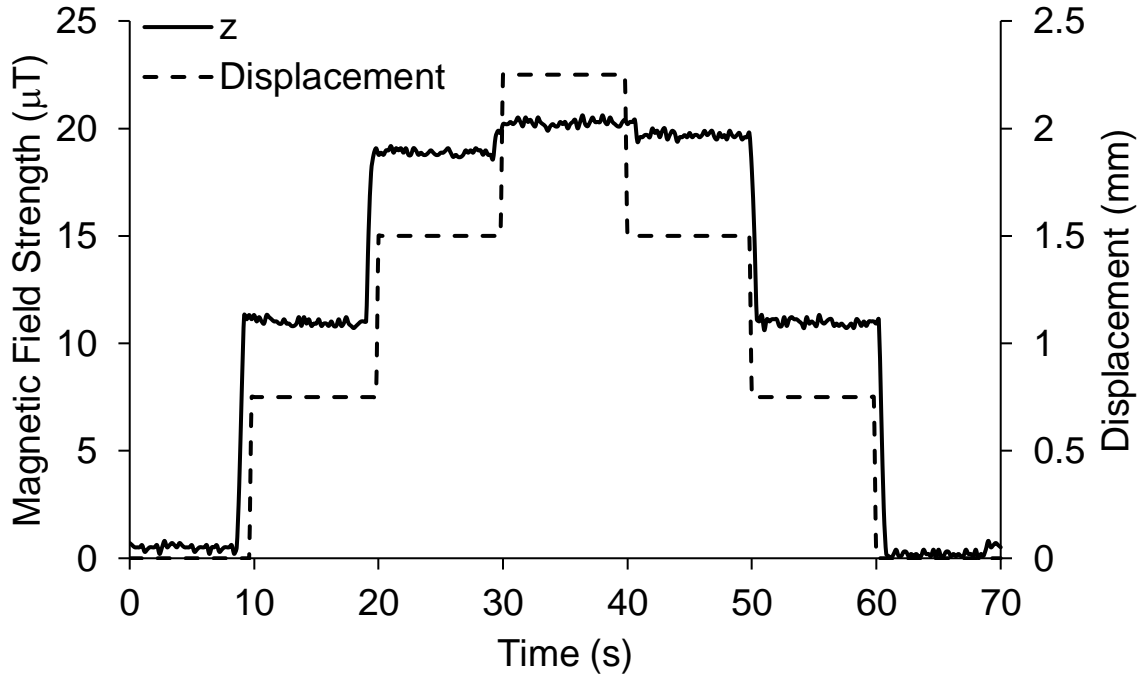


Figure 23: Preliminary results of field strength (displayed from the z axis) and the displacement versus time of 1 wt % nickel.

During our initial evaluations, we were able to identify the magnetic field strength of nickel, carbonyl iron, iron oxide, and magnetite at 1 wt % within PDMS when displaced a total of 2.25 mm. Nickel provided a very strong magnetic field response of 20.25 μT (Figure 24). Iron oxide and magnetite also displayed viable responses of 9.32 and 5.35 μT , respectively. A preliminary objective of this study was to deliver a sensitivity analysis of the lowest concentration (wt %) possible to observe a change in magnetic field strength from these ferromagnetic materials. From the initial studies depicted in Figure 24, we can see that 1 wt % carbonyl iron only provided a response of 1.08 μT when displaced 2.25 mm by the stepper motor whereas, as illustrated in Figure 17, it only displayed a response of 2.46 μT when displaced 1.14

mm by 600 g of force from the ElectroForce. Both of these responses were relatively close to the blank PDMS cylinders which displayed a magnetic field response of 0.61 μT in Figure 24 and 2.27 μT in Figure 17. This helped us determine that carbonyl iron is not providing a reliable magnetic field response when compressed and these values were likely background interference.

Similarities between the iron oxide and magnetite were evident from the initial evaluations (Figure 24). Based on the results depicted in Figure 17 and Figure 19, we can see that magnetite displayed a magnetic field response of 4.11 μT when it was displaced 1.44 mm by 600 g of force. The iron oxide also provided a magnetic field response of 5.33 μT when displaced 1.45 mm by the same amount of force. If we look at the 1.50 mm bar in Figure 24, we can see magnetite and iron oxide produced magnetic field responses of 3.17 and 7.58 μT , respectively, which is consistent with the results seen with the ElectroForce.

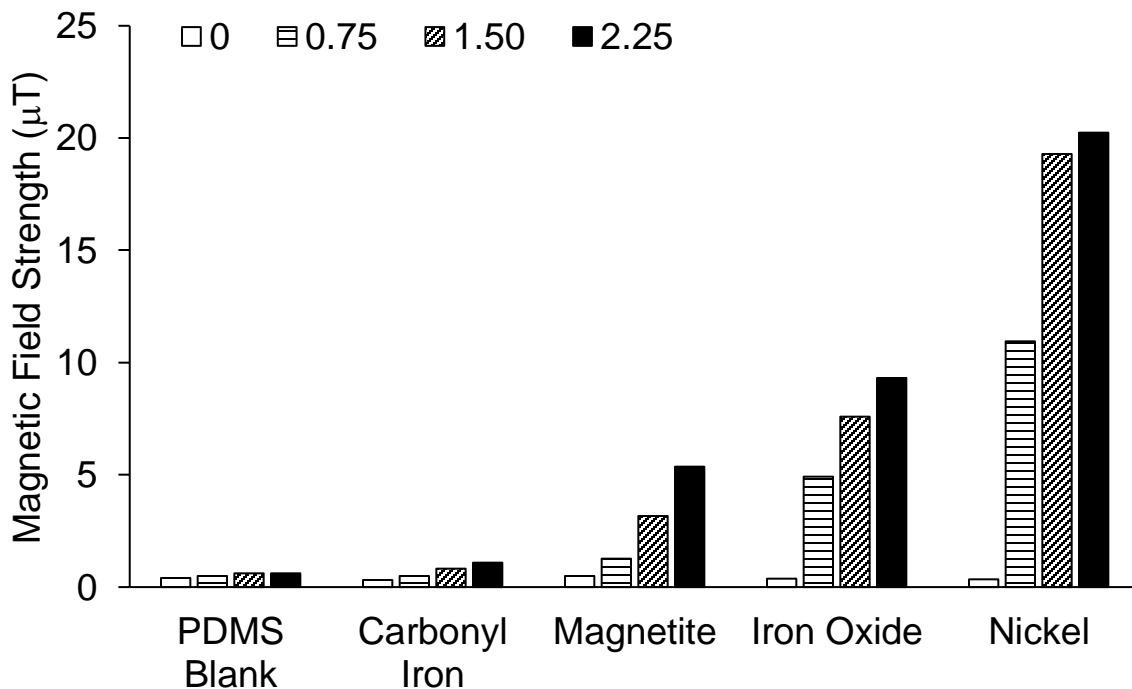


Figure 24: Magnetic field strength from materials studied during preliminary trials at 1 wt % during 0, 0.75, 1.50, and 2.25 mm of displacement.

As seen from Figure 25, the lowest wt % possible for detection of these ferromagnetic fillers occurred at 1 wt % concentration for this study. At 600 g of force, neodymium and nickel only displayed readings of 2.80 and 2.22 μT at 0.1 wt %, respectively, compared to PDMS which displayed a magnetic response of 2.27 μT at 600 g of force. The remaining magnetic materials also all displayed responses below 3 μT at 0.1 wt %. This was not a reliable response for detecting magnetic field strength within constructs at 0.1 wt % or lower at 0.01 wt %.

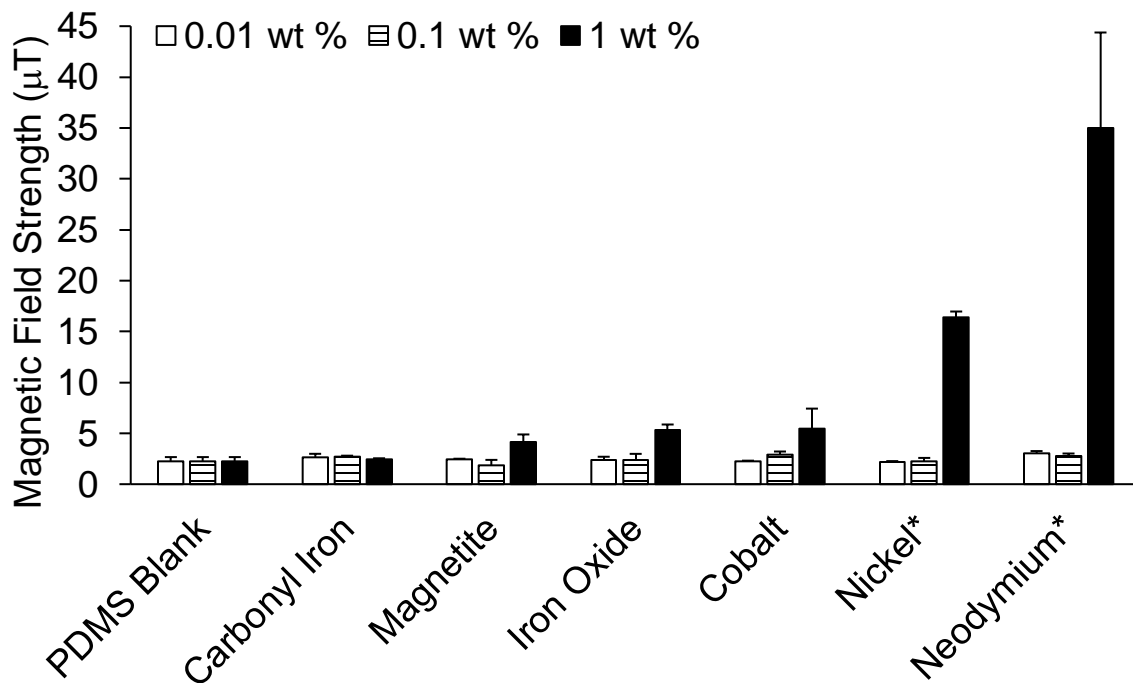


Figure 25: Magnetic field strength of all six magnetic fillers at 0.01, 0.1, and 1 wt % during 600 g of force. * denotes statistical difference from PDMS at 1 wt % and at 600 g of force ($p < 0.0001$).

The displacements of each magnetic filler material at each wt % was observed when 600 g of compressive force was applied to determine compressive strengths within PDMS. We originally hypothesized that the magnetic materials would increase the compressive modulus of PDMS, therefore making each sample more resistive to displacement as filler content increased. However, as seen in Figure 26, we can see there are inconsistent trends of displacement between

separate magnetic materials at varying wt %'s. There are a few possible causes for such altered displacements between samples. Most notably, if the w/w ratio of silicone base to curing agent is altered slightly from 15:1, this would affect material stiffness. If the ratio is lowered, the silicone will develop a higher compressive strength and be more resistive to displacement. On the other hand, if the ratio is increased, the cured silicone will have a lower compressive strength and be displaced more⁴⁰.

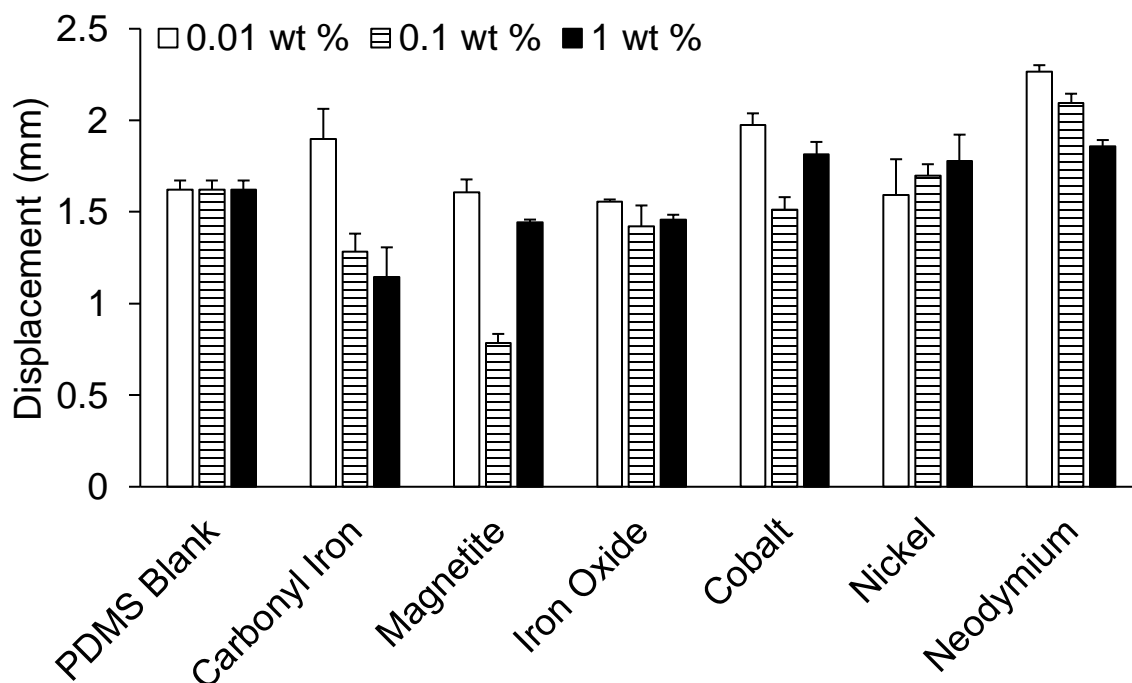


Figure 26: Displacement of all six magnetic fillers at 0.01, 0.1, and 1 wt % during 600 g of force.

Additional studies were conducted to explore a magnetic filler material within other soft materials. Due to its abundance and relatively low cost, iron oxide was selected as the ferromagnetic compound to be mixed with BJB, DMS-V21, and DMS-V33. Figure 27 displays the magnetic field response from the blank soft materials with no iron oxide to establish a baseline as well as the samples with 1 wt % iron oxide. PDMS showed the highest response in magnetic field with 1 wt % iron oxide with an average reading of 5.33 μ T at 600 g of

compressive force. DMS-V21 presented the second highest response of 4.35 μT while DMS-V33 and BJB displayed a response of 3.41 and 2.41 μT at 600 g of force, respectively. Notably, BJB showed no promise as a soft material, but this is because the material did not compress at 600 g of force. Figure 28 shows that the BJB-Blank and BJB-iron oxide samples were only displaced an average of 0.58 and 0.41 mm, respectively. Although the DMS-V21 and DMS-V33 showed some promise, it should be noted that the blank samples of these silicones displayed higher average magnetic readings than the PDMS and BJB. This could be due to a greater magnetic background interference from the ElectroForce's top geometry for these samples. The average displacement of the blank DMS-V21 samples were more than twice as large as the DMS-V33 and PDMS blanks. With the displacement of the DMS-V21 and DMS-V33 samples being larger than that of the PDMS, it would have also been expected that the magnetic field response of these silicones would also have been larger than PDMS when iron oxide at 1 wt % was incorporated. However, this was not the case as the PDMS-iron oxide still showed the greatest magnetic field response. Therefore, it is hypothesized that the platinum catalyst may have played a role in altering magnetic strength readings within the DMS-V21 and DMS-V33. Using two-way ANOVA, there was no statistical difference observed in any of these samples except when using the Dunnett method to compare the DMS-V21-iron oxide and PDMS-iron oxide samples compared to the blank PDMS samples ($p < 0.03$).

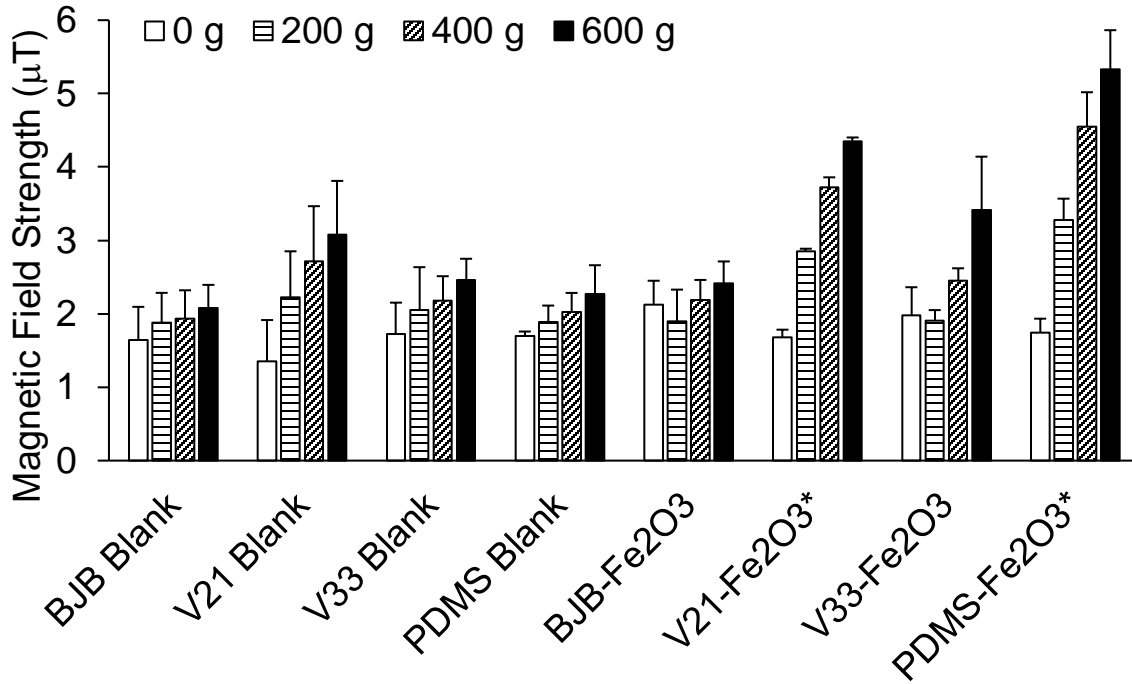


Figure 27: Magnetic field strength of blank soft materials and soft materials with 1 wt % iron oxide during 0, 200, 400, and 600 g of force. * denotes statistical difference from PDMS Blank at 600 g of force ($p < 0.03$).

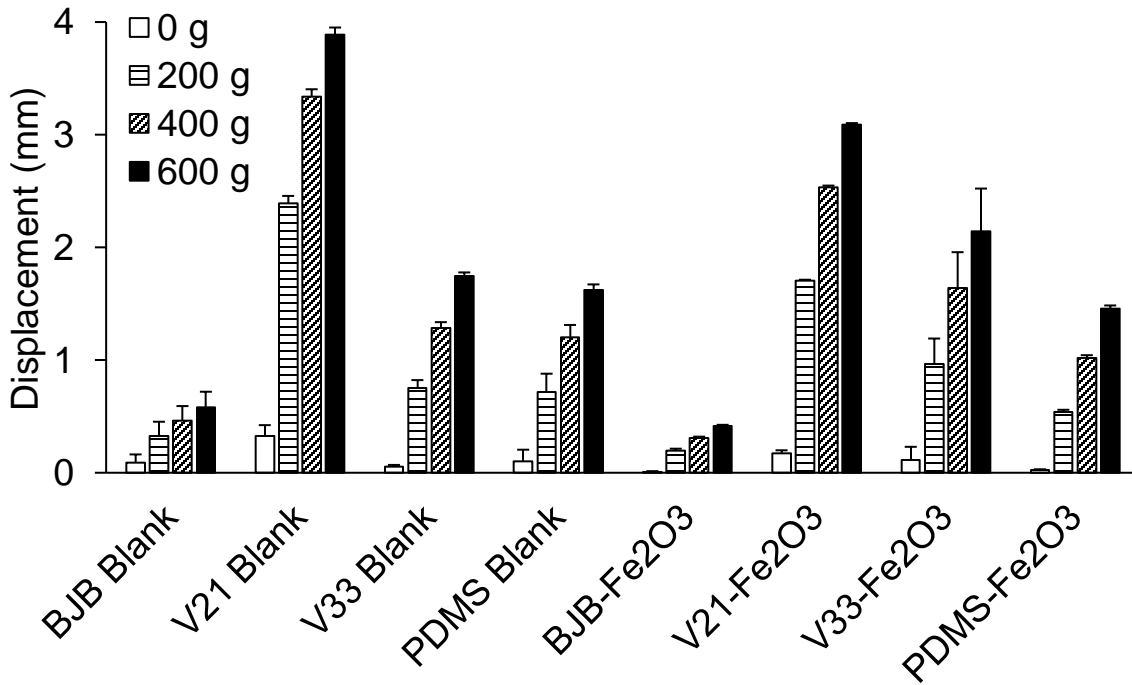


Figure 28: Displacement of blank soft materials and soft materials with 1 wt % iron oxide during 0, 200, 400, and 600 g of force.

Although DMS-V21 also seemed that it would show some promise as a potential material for soft sensors, when we view Figure 29, we can see that it does not have much compressive strength. In fact, compression cycles were originally intended to go up to 750 g of force, but DMS-V21 samples would fail around 700-750 g of force.

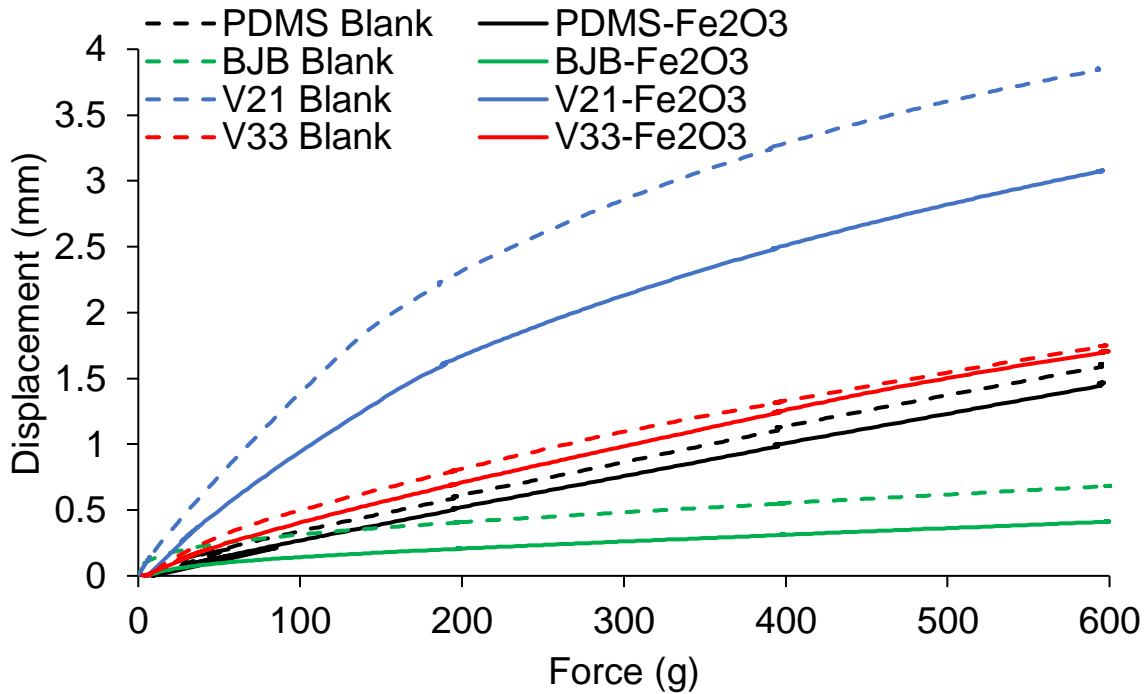


Figure 29: Displacement as a function of force for one sample (n=1) of each soft material with and without 1 wt % iron oxide. Only the compression cycles are displayed here.

Settling velocities of magnetic particles was also investigated, since settling became evident during mixing of neodymium within PDMS at 1 wt %. In order to calculate settling time and viscosities, densities and viscosities of the siloxanes and their curing agent at specific weight-to-weight ratios were required. Mixture density, ρ , was calculated as the summation of the mass fraction, x , multiplied by the density of each component as seen in Equation 142.

$$\rho_n = \sum (x_i * \rho_i)_n \quad (1)$$

Equation 2 was used to calculate the natural log of the mixture viscosity, η , as the natural log of each component's viscosity multiplied by its mass fraction⁴³.

$$\ln \eta = x_1 \ln \eta_1 + x_2 \ln \eta_2 \quad (2)$$

Table 4 provides the estimated densities and viscosities of DMS-V21, DMS-V33, and PDMS calculated from Equations 1 and 2 at a 15:1 w/w ratio with Sylgard 184 curing agent.

Table 4: Estimated mixture densities and viscosities of silicones at 15:1 w/w ratio with Sylgard 184 curing agent.

Soft Material	Estimated Mixture Density (kg/m³)	Estimated Mixture Viscosity (cSt)
DMS-V21	975	100
DMS-V33	975	2,820
PDMS	1105	3,940

After mixture densities and viscosities were determined, settling velocity, v , was estimated using Stokes Law. Assumptions were made before estimating each settling velocity. These assumptions were as follows: laminar flow where the Reynolds number is less than 0.3, homogenous mixtures, particles were spherical with smooth surfaces, and no particle-particle interactions. These assumptions combined to form Equation 3 from Stokes Law to solve for the settling viscosities of carbonyl iron, iron oxide, magnetite, and neodymium⁴⁴.

$$v = \frac{2(\rho_p - \rho_s)}{9\mu} gR^2 \quad (3)$$

Since nickel and cobalt were both cylindrical, a modified relationship from Stokes Law of flow of spherical particles is formed⁴⁵. Equation 4 accounts for the correlation between the cylinder's length, L , and diameter, D .

$$v = \frac{0.0790(\rho_p - \rho_s)}{\mu} gL^2 \left(\frac{L}{D}\right)^{-1.664} \quad (4)$$

Figure 30 presents the estimated settling velocity of all six ferromagnetic particles within a varying range of viscosity from 100-4,170 cSt. All of the materials except for the neodymium

display a settling velocity of less than 0.40 mm/min in solutions with a viscosity of 100 cSt. Therefore, these particles were all considered to have settling velocities near zero within PDMS during the curing process. Even iron oxide's settling velocity was approximately zero within DMS-V21, which had an estimated viscosity of 100 cSt. However, the neodymium displays a settling velocity range from 0.60 mm/min to 25.60 mm/min in solutions with a viscosity of nearly 4,170 and 100 cSt, respectively. Therefore, neodymium's settling velocity could not be ignored during the curing process as it would take about 15 minutes for neodymium particles to settle within PDMS with a viscosity of 4,000 cSt.

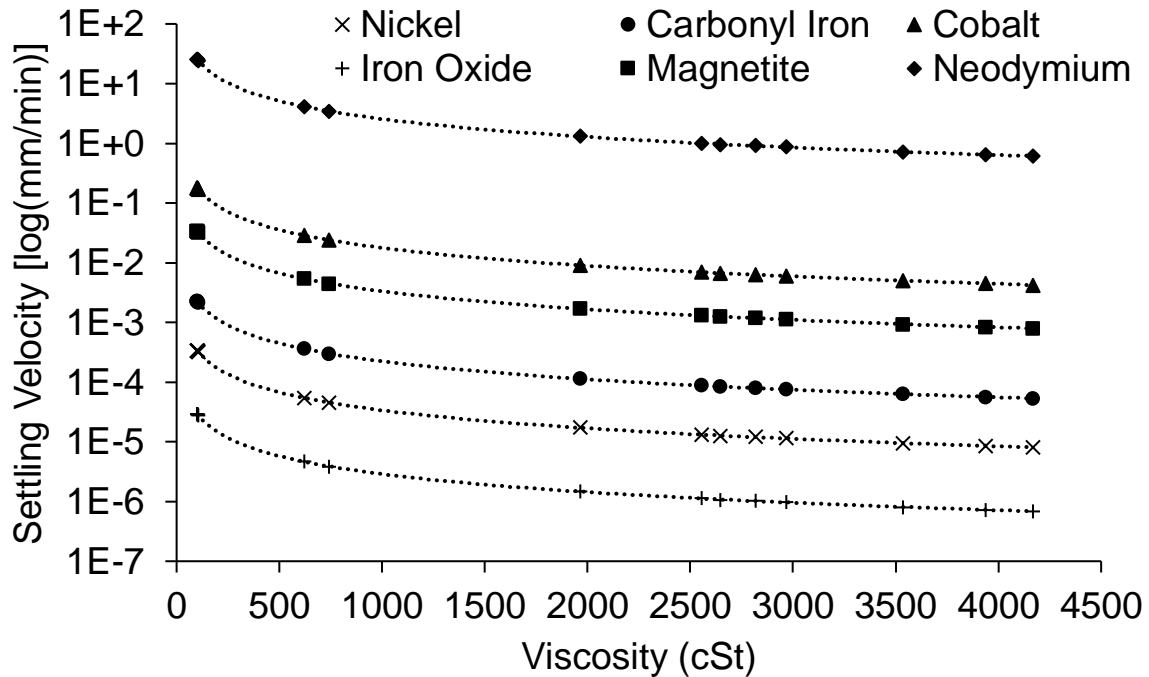


Figure 30: Estimated settling velocities of magnetic particles within solutions of varying viscosities.

The neodymium had an average particle size of 50-60 μm so we wanted to investigate the acceptable range of particle sizes within varying viscosities so that neodymium's settling velocity could then be assumed to zero. Figure 31 presents an estimated settling velocity for varying particle sizes of neodymium of 0, 25, 50, 75, and 100 μm in solutions with a viscosity

range of 100-4,170 cSt. Only neodymium particle sizes of 25 μm or less could be considered to have an assumed settling velocity of approximately zero in solutions with a viscosity of 2,000 cSt or more.

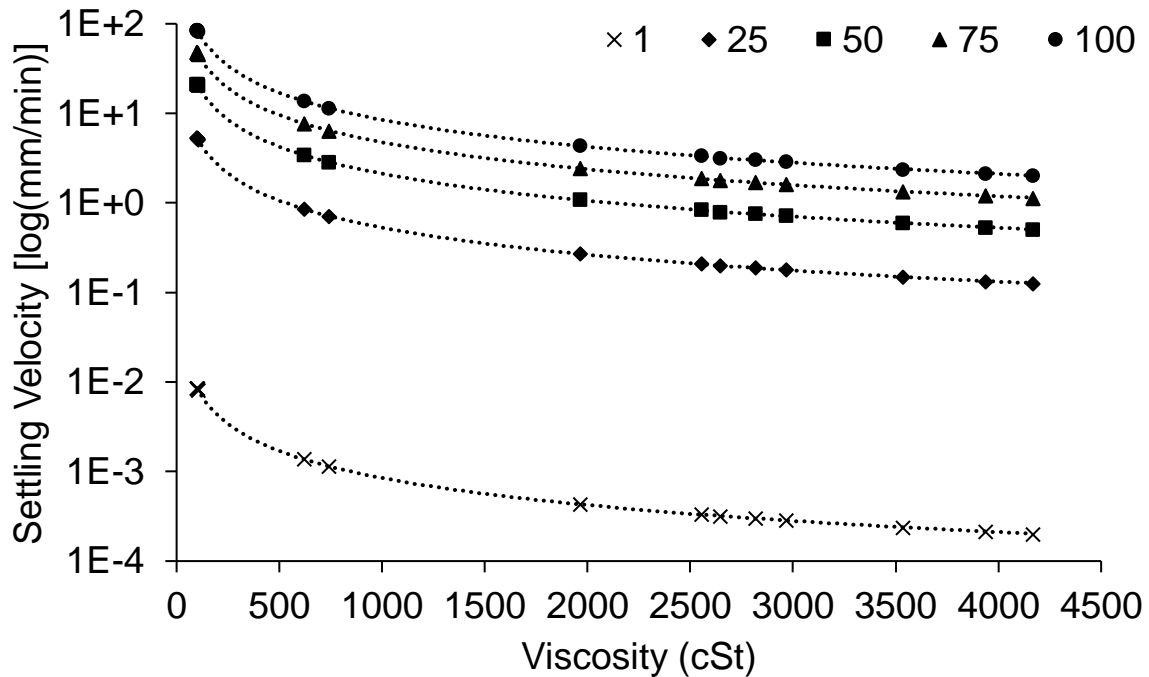


Figure 31: Estimated settling velocities of differing particle sizes (1, 25, 50, 75, and 100 mm) of neodymium within solutions of varying viscosities.

The volume percent (vol %) is important to understand when dealing with particles at the micro and nanoscale. Using the ferromagnetic and soft materials' densities, it's possible to convert from wt % to vol %. Table 5 displays the calculated vol % of each magnetic material at the within PDMS at each various wt %. The vol % of iron oxide within each soft material was also converted from 1 wt % (Table 6).

Table 5: Volume % of ferromagnetic fillers within PDMS at each wt %.

Material	Vol %		
	0.01 wt %	0.1 wt %	1 wt %
Carbonyl Iron	1.41E-03	1.41E-02	1.42E-01
Cobalt	1.24E-03	1.24E-02	1.25E-01
Iron Oxide	2.23E-03	2.23E-02	2.25E-01
Magnetite	2.17E-03	2.17E-02	2.18E-01
Neodymium	1.47E-03	1.47E-02	1.49E-01
Nickel	1.24E-03	1.24E-02	1.25E-01

Table 6: Vol % of iron oxide within each soft material.

Soft Material	Vol % of Iron Oxide
BJB	2.13E-01
PDMS	2.25E-01
DMS-V21	1.98E-01
DMS-V33	1.98E-01

Conclusions

We were able to identify that 1 wt % was the minimum required concentration of magnetic filler to detect a magnetic response from compressive forces and displacement for nickel nanorods, cobalt nanowires, iron oxide nanopowder, magnetite powder, and neodymium powder incorporated within PDMS though a statistical difference was only observed with nickel and neodymium. However, this was not the case for the carbonyl iron microspheres integrated within PDMS as there was no viable magnetic response generated at 1 wt %.

Overall, the 1 wt % neodymium-PDMS cylindrical constructs showed the greatest magnetic field response when compressed at 600 g of force. However, the particles were also much larger than the other magnetic materials. Even in PDMS at a 15:1 w/w ratio of base to curing agent, which has an approximate viscosity of 3,900-4,000 cSt, the neodymium settled at a rate of 0.64 mm/min. Therefore, moving forward, smaller neodymium particles should be evaluated.

The PDMS also displayed the most desirable properties and relationship between force and displacement with and without the magnetic fillers. Without any magnetic materials incorporated, the PDMS and DMS-V21 exhibited similar Young's moduli which were the most favorable as they were compressible, unlike the BJB, but they were also resistive enough to not reach their ultimate strength at lower forces like the DMS-V21. However, the PDMS was more desirable than the DMS-V33 because of the magnetic field response generated when 1 wt % iron oxide was incorporated into the materials and compressed.

Chapter 3: Future Directions

Investigations into ferromagnetic fillers and sensors that may guide the next generation of smart wireless sensors is on-going and based on emerging findings provides many avenues of further assessments, refinements of techniques, and selection of investigative materials. Moving forward, we would like to focus on performing similar force and displacement tests that were previously executed by the ElectroForce, but rather than placing the triple axis accelerometer and magnetometer directly between the bottom of the cylindrical samples and the bottom of the ElectroForce geometry, we envision implementing a structure to support the magnetometer directly perpendicular to the sample and the ElectroForce. In the current assessment, the cross-sectional area of the actual sensor on the magnetometer board is much smaller than the cross-sectional area of the cylinders. As a result, the outcomes may have been affected by the cylindrical constructs beginning to engulf the sensor itself as the ElectroForce continuously displaced the sample.

Although the neodymium powder displayed the strongest magnetic field response, it was also the largest particle compared to the nickel nanorods, carbonyl iron microspheres, cobalt nanowires, and iron oxide nanopowder, magnetite powder. Therefore, they displayed a settling rate far exceeding the other materials. Since it cannot be assumed that the settling rate of neodymium was zero during the curing process, it would be important for further investigations to assess the magnetic field strength of neodymium particles at a much smaller size, on the order of 25 μm or less.

In further investigations, rheological analyses will be vital in understanding the ability that these ferromagnetic fillers have on additive manufacturing techniques such as 3D printing. Although a certain magnetic particle like the neodymium displayed favorable magnetic field

response, it may not be favorable for 3D printing techniques such as DIW. In order to display the rheological prerequisites for desirable 3D printing techniques like DIW, the inks need to be of suitable sizes as not to obstruct the extrusion heads during manufacturing. Inks also need to have a certain viscosity range of 0.1 to 1,000 Pa/s^{35, 46-48}. Therefore, it would be important to continue analyzing different magnetic materials at altered wt %'s and within varying viscous silicones (i.e., DMS-V21, DMS-V33, and PDMS with varying w/w ratios of base to curing agent).

Investigating these different silicones at varying w/w ratios would provide important information. Our findings and those of others suggest that even if certain ratios of each silicone composite display similar viscosities, their storage and loss moduli may still be very different. DIW inks need to have the ability to flow at a lower viscosity when placed under a shear force, meaning that the loss modulus needs to be greater than the storage modulus. However, it's imperative that DIW inks then have the ability to rapidly heal after extrusion so they recover after the shear force is removed, which means the storage modulus is now greater than the loss modulus. The faster the recovery, the more desirable the ink becomes especially since shear thinning are extremely common in soft materials³⁶.

Aside from utilizing these magnetically infused polymers in DIW printing, we would also like to explore the ability of incorporating these ferromagnetic materials into photopolymerizable resins. This would explore the ability to print magnetic structures from these resins through stereolithography (SLA) printing. Minor inquiries were made into incorporating magnetic fillers into resins, but they became too opaque to crosslink at heights above 2-3 mm using an ultraviolet lamp. Future investigations would include the ability to an electromagnet within the SLA printer as well as printing or crosslinking in smaller and more consistent heights of about 100 μm .

The next investigative step would be to consider the usage of a wireless triple axis accelerometer and magnetometer via Bluetooth or another wireless connection. This would allow for the possibility to incorporate sensors directly into the silicones or polymers themselves. Larger constructs could be built in 12 well plates or even petri dishes depending on the size of the remote wireless magnetometer. There is then the possibility of integrating these larger constructs into shoe soles to detect the displacement and force of the person walking based on the magnetic field strength generated from the magnetic particles that are then detected from the sensor within the composite. However, because the placement of the sensor-containing composite in the sole faces repeated force and displacement, it may also be better to place the wireless magnetometer in close proximity to the magnetic composite (i.e., the tongue of the shoe) as to not break the sensor due to repeated compression of the shoe soles. In this case, it would also be important to develop a more formal relationship between the force and displacement of the materials against their magnetic field response. That way, the force and the displacement could be determined from the magnetic field response received by the magnetometer. This technology could be then utilized to help predict possible injuries from repeated stress and strain within people and potentially professional athletes.

Among the wide range of possible directions for further investigations, an assessment of the magnetic composite's ability to reconnect soft tissue may offer important clinical benefits for patients with soft tissue disorders. Self-healing hydrogels with pressure sensitivity and stretchability are novel concepts that are just recently being discovered.

References

1. Frutiger, A.; Muth, J. T.; Vogt, D. M.; Mengüç, Y.; Campo, A.; Valentine, A. D.; Walsh, C. J.; Lewis, J. A., Capacitive Soft Strain Sensors via Multicore–Shell Fiber Printing. *Advanced Materials* **2015**, *27* (15), 2440-2446.
2. Martin, J. J.; Fiore, B. E.; Erb, R. M., Designing bioinspired composite reinforcement architectures via 3D magnetic printing. *Nature Communications* **2015**, *6* (1), 8641.
3. Darabi, M. A.; Khosrozadeh, A.; Mbeleck, R.; Liu, Y.; Chang, Q.; Jiang, J.; Cai, J.; Wang, Q.; Luo, G.; Xing, M., Skin-Inspired Multifunctional Autonomic-Intrinsic Conductive Self-Healing Hydrogels with Pressure Sensitivity, Stretchability, and 3D Printability. *Advanced Materials* **2017**, *29* (31), 1700533.
4. Zeng, W.; Shu, L.; Li, Q.; Chen, S.; Wang, F.; Tao, X. M., Fiber-Based Wearable Electronics: A Review of Materials, Fabrication, Devices, and Applications. *Advanced Materials* **2014**, *26* (31), 5310-5336.
5. Pang, C.; Lee, C.; Suh, K. Y., Recent advances in flexible sensors for wearable and implantable devices. 2013; Vol. 130, pp 1429-1441.
6. Vaidya, U. K.; Chawla, K. K., Processing of fibre reinforced thermoplastic composites. 2008; Vol. 53, pp 185-218.
7. Mouritz, A. P.; Bannister, M. K.; Falzon, P. J.; Leong, K. H., Review of applications for advanced three-dimensional fibre textile composites. *Composites Part A* **1999**, *30* (12), 1445-1461.
8. Benjamin, C. K. T.; Chao, W.; Ranulfo, A.; Zhenan, B., An electrically and mechanically self-healing composite with pressure- and flexion-sensitive properties for electronic skin applications. *Nature Nanotechnology* **2012**, *7* (12), 825.
9. Rashid, A.; Hasan, O., Wearable technologies for hand joints monitoring for rehabilitation: A survey. *Microelectronics Journal* **2019**, *88*, 173-183.
10. Mirzanejad, H.; Agheli, M., Soft force sensor made of magnetic powder blended with silicone rubber. *Sensors and Actuators A: Physical* **2019**, *293*, 108-118.
11. Mirzanejad, H.; Tabrizi, M. M.; Fathian, A.; Sharifnejad, A.; Agheli, M. In *A New Soft Force Sensor using Blended Silicone-Magnetic powder*, 2017 5th RSI International Conference on Robotics and Mechatronics (ICRoM), 25-27 Oct. 2017; 2017; pp 150-155.
12. Hongbo, W.; de Boer, G.; Junwai, K.; Alazmani, A.; Ghajari, M.; Hewson, R.; Culmer, P., Design Methodology for Magnetic Field-Based Soft Tri-Axis Tactile Sensors. *Sensors (14248220)* **2016**, *16* (9), 1356.
13. Jamone, L.; Metta, G.; Nori, F.; Sandini, G. In *James: A Humanoid Robot Acting over an Unstructured World*, 2006 6th IEEE-RAS International Conference on Humanoid Robots, 4-6 Dec. 2006; 2006; pp 143-150.
14. Kou, H.; Zhang, L.; Tan, Q.; Liu, G.; Dong, H.; Zhang, W.; Xiong, J., Wireless wide-range pressure sensor based on graphene/PDMS sponge for tactile monitoring. *Scientific Reports* **2019**, *9* (1), 3916.
15. Alex, C.; Jia, L.; Zhenan, B., Pursuing prosthetic electronic skin. *Nature Materials* **2016**, *15* (9).
16. Ho-Hsiu, C.; Amanda, N.; Alex, C.; John, W. F. T.; Chien, L.; Jianguo, M.; Tadanori, K.; Won-Gyu, B.; Jeffrey, B. H. T.; Zhenan, B., A chameleon-inspired stretchable electronic skin with interactive colour changing controlled by tactile sensing. *Nature Communications* **2015**, *6* (1).

17. Wang, X.; Gu, Y.; Xiong, Z.; Cui, Z.; Zhang, T., Silk-Molded Flexible, Ultrasensitive, and Highly Stable Electronic Skin for Monitoring Human Physiological Signals. *Advanced Materials* **2014**, *26* (9), 1336-1342.
18. Ho, D. H.; Sun, Q.; Kim, S. Y.; Han, J. T.; Kim, D. H.; Cho, J. H., Stretchable and Multimodal All Graphene Electronic Skin. *Advanced Materials* **2016**, *28* (13), 2601-2608.
19. Donghee, S.; Jongha, L.; Shutao, Q.; Roozbeh, G.; Jaemin, K.; Ji Eun, L.; Changyeong, S.; Seok Joo, K.; Dong Jun, L.; Samuel Woojoo, J.; Shixuan, Y.; Minjoon, P.; Jiho, S.; Kyungsik, D.; Mincheol, L.; Kwanghun, K.; Cheol Seong, H.; Nanshu, L.; Taeghwan, H.; Dae-Hyeong, K., Multifunctional wearable devices for diagnosis and therapy of movement disorders. *Nature Nanotechnology* **2014**, *9* (5), 397.
20. Patel, M. S.; Asch, D. A.; Volpp, K. G., Wearable Devices as Facilitators, Not Drivers, of Health Behavior Change. *JAMA* **2015**, *313* (5).
21. Haghi, M.; Thurow, K.; Stoll, R., Wearable Devices in Medical Internet of Things: Scientific Research and Commercially Available Devices. *Healthcare informatics research* **2017**, *23* (1), 4-15.
22. Kappassov, Z.; Corrales, J.-A.; Perdereau, V., Tactile sensing in dexterous robot hands — Review. *Robotics and Autonomous Systems* **2015**, *74*, 195-220.
23. Kyberd, P. J.; Chappell, P. H., A force sensor for automatic manipulation based on the Hall effect. *Measurement Science and Technology* **1993**, *4* (3), 281-287.
24. Low, J. H.; Khin, P. M.; Yeow, C. H. In *A pressure-redistributing insole using soft sensors and actuators*, 2015 IEEE International Conference on Robotics and Automation (ICRA), 26-30 May 2015; 2015; pp 2926-2930.
25. Mengüç, Y.; Park, Y.; Martinez-Villalpando, E.; Aubin, P.; Zisook, M.; Stirling, L.; Wood, R. J.; Walsh, C. J. In *Soft wearable motion sensing suit for lower limb biomechanics measurements*, 2013 IEEE International Conference on Robotics and Automation, 6-10 May 2013; 2013; pp 5309-5316.
26. Chathuranga, D. S.; Wang, Z.; Noh, Y.; Nanayakkara, T.; Hirai, S. In *Disposable soft 3 axis force sensor for biomedical applications*, 2015 37th Annual International Conference of the IEEE Engineering in Medicine and Biology Society (EMBC), 25-29 Aug. 2015; 2015; pp 5521-5524.
27. Hallali, N.; Clerc, P.; Fourmy, D.; Gigoux, V.; Carrey, J., Influence on cell death of high frequency motion of magnetic nanoparticles during magnetic hyperthermia experiments. *Applied Physics Letters* **2016**, *109* (3), 032402.
28. Lee, J.-J.; Jeong, K. J.; Hashimoto, M.; Kwon, A. H.; Rwei, A.; Shankarappa, S. A.; Tsui, J. H.; Kohane, D. S., Synthetic Ligand-Coated Magnetic Nanoparticles for Microfluidic Bacterial Separation from Blood. *Nano Letters* **2014**, *14* (1), 1-5.
29. Liu, L.; Yu, P.; Zhang, Y.; Wu, B.; Cui, C.; Wu, M.; Wang, C.-X.; Zhuo, R.-X.; Huang, S.-W., Doxorubicin-conjugated magnetic iron oxide nanoparticles for pH-sensitive and magnetic responsive drug delivery. *Journal of Controlled Release* **2015**, *213*, e67-e67.
30. Frey, N. A.; Peng, S.; Cheng, K.; Sun, S., Magnetic nanoparticles: synthesis, functionalization, and applications in bioimaging and magnetic energy storage. *Chemical Society Reviews* **2009**, *38* (9), 2532-2542.
31. Jedlovszky-Hajdú, A.; Tombácz, E.; Bányai, I.; Babos, M.; Palkó, A., Carboxylated magnetic nanoparticles as MRI contrast agents: Relaxation measurements at different field strengths. *Journal of Magnetism and Magnetic Materials* **2012**, *324* (19), 3173-3180.

32. Schwartz, G.; Tee, B. C. K.; Mei, J.; Appleton, A. L.; Kim, D. H.; Wang, H.; Bao, Z., Flexible polymer transistors with high pressure sensitivity for application in electronic skin and health monitoring. *Nature Communications* **2013**, *4* (1), 1859.
33. Puangmali, P.; Liu, H.; Seneviratne, L. D.; Dasgupta, P.; Althoefer, K., Miniature 3-Axis Distal Force Sensor for Minimally Invasive Surgical Palpation. *IEEE/ASME Transactions on Mechatronics* **2012**, *17* (4), 646-656.
34. Chatzipirpiridis, G.; Erne, P.; Ergeneman, O.; Pané, S.; Nelson, B. J. In *A magnetic force sensor on a catheter tip for minimally invasive surgery*, 2015 37th Annual International Conference of the IEEE Engineering in Medicine and Biology Society (EMBC), 25-29 Aug. 2015; 2015; pp 7970-7973.
35. Paxton, N.; Smolan, W.; Böck, T.; Melchels, F.; Groll, J.; Jungst, T., Proposal to assess printability of bioinks for extrusion-based bioprinting and evaluation of rheological properties governing bioprintability. *Biofabrication* **2017**, *9* (4), 044107.
36. Chen, D. T. N.; Wen, Q.; Janmey, P. A.; Crocker, J. C.; Yodh, A. G., Rheology of Soft Materials. *Annual Review of Condensed Matter Physics* **2010**, *1* (1), 301-322.
37. Gul, J. Z.; Sajid, M.; Rehman, M. M.; Siddiqui, G. U.; Shah, I.; Kim, K.-H.; Lee, J.-W.; Choi, K. H., 3D printing for soft robotics - a review. *Sci Technol Adv Mater* **2018**, *19* (1), 243-262.
38. Kim, Y.; Yuk, H.; Zhao, R.; Chester, S. A.; Zhao, X., Printing ferromagnetic domains for untethered fast-transforming soft materials. *Nature* **2018**, *558* (7709), 274-279.
39. Schmid, H.; Michel, B., Siloxane Polymers for High-Resolution, High-Accuracy Soft Lithography. *Macromolecules* **2000**, *33* (8), 3042-3049.
40. Wang, Z.; Volinsky, A. A.; Gallant, N. D., Crosslinking effect on polydimethylsiloxane elastic modulus measured by custom-built compression instrument. *Journal of Applied Polymer Science* **2014**, *131* (22).
41. Bentley, A. K.; Farhoud, M.; Ellis, A. B.; Nickel, A.-M. L.; Lisensky, G. C.; Crone, W. C., Template Synthesis and Magnetic Manipulation of Nickel Nanowires. *Journal of Chemical Education* **2005**, *82* (5), 765.
42. Perry, R.; Green, D., *Perry's Chemical Engineers' Handbook, Eighth Edition*. McGraw-Hill Education: 2008.
43. Bloomfield, V. A.; Dewan, R. K., Viscosity of liquid mixtures. *The Journal of Physical Chemistry* **1971**, *75* (20), 3113-3119.
44. Lamb, H., *Hydrodynamics*. Dover publications: New York, 1945.
45. Komar, P. D., Settling Velocities of Circular Cylinders at Low Reynolds Numbers. *The Journal of Geology* **1980**, *88* (3), 327-336.
46. Li, L.; Lin, Q.; Tang, M.; Duncan, A. J. E.; Ke, C., Advanced Polymer Designs for Direct-Ink-Write 3D Printing. *Chemistry – A European Journal* **2019**, *25* (46), 10768-10781.
47. Hölzl, K.; Lin, S.; Tytgat, L.; Van Vlierberghe, S.; Gu, L.; Ovsianikov, A., Bioink properties before, during and after 3D bioprinting. *Biofabrication* **2016**, *8* (3), 032002.
48. Lewis, J. A., Direct Ink Writing of 3D Functional Materials. *Advanced Functional Materials* **2006**, *16* (17), 2193-2204.

Appendix

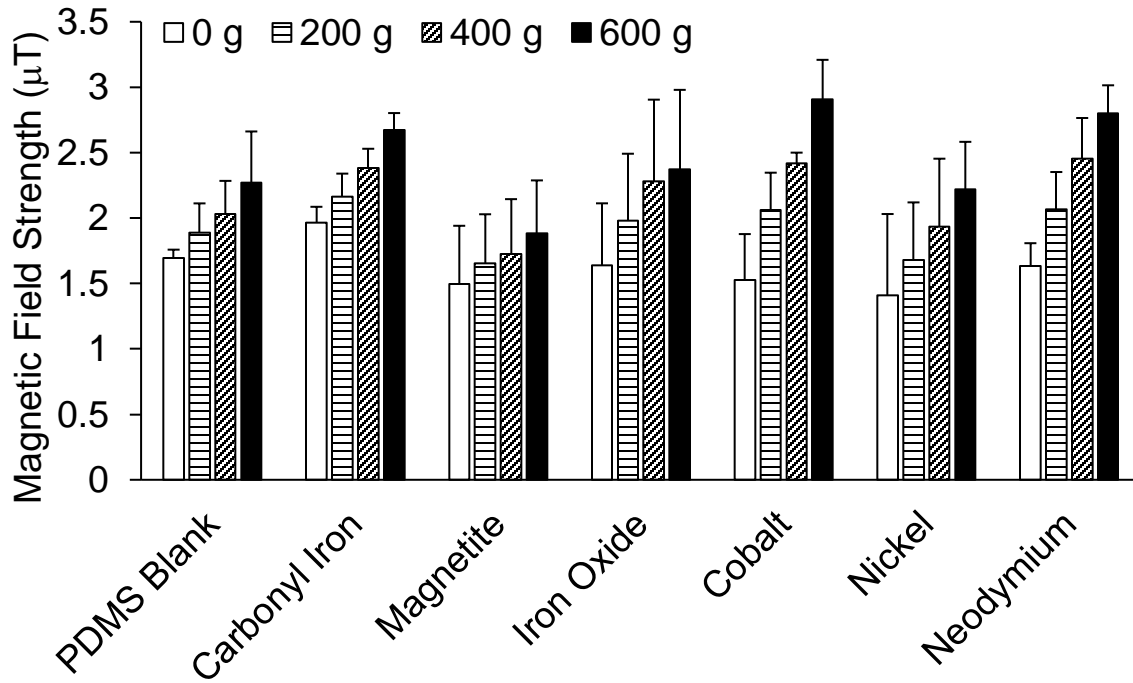


Figure 32: Magnetic field strength from all six magnetic fillers at 0.1 wt % during 0, 200, 400, and 600 g of force.

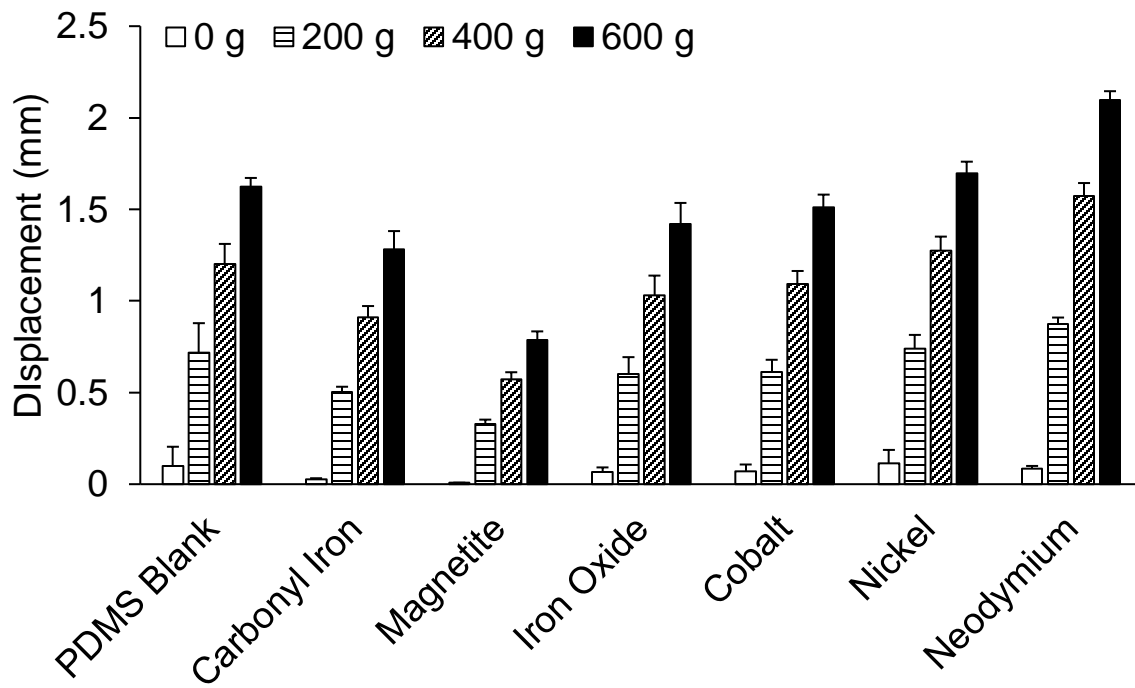


Figure 33: Displacement of all six magnetic fillers at 0.1 wt % during 0, 200, 400, and 600 g of force.

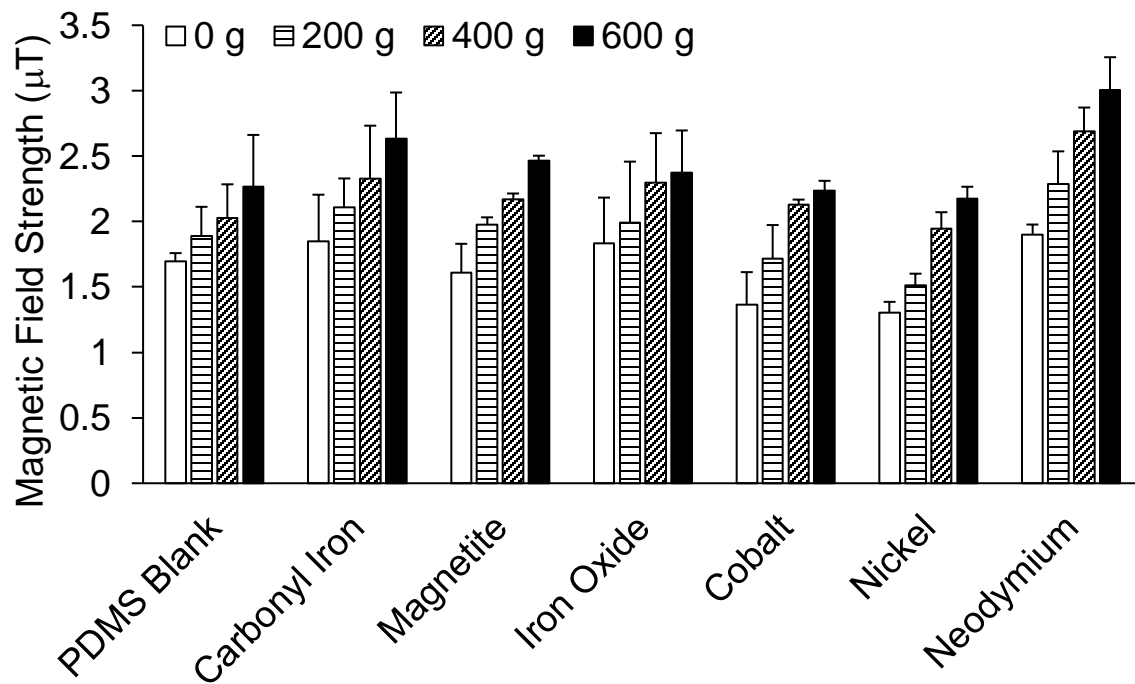


Figure 34: Magnetic field strength from all six magnetic fillers at 0.01 wt % during 0, 200, 400, and 600 g of force.

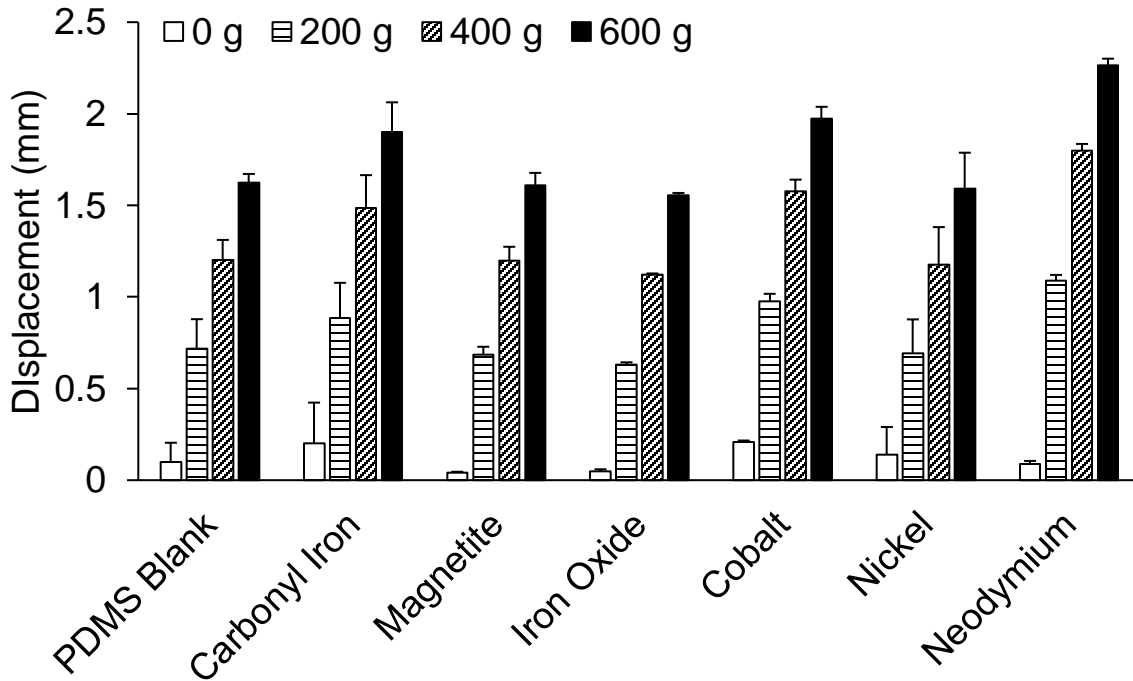


Figure 35: Displacement of all six magnetic fillers at 0.01 wt % during 0, 200, 400, and 600 g of force.

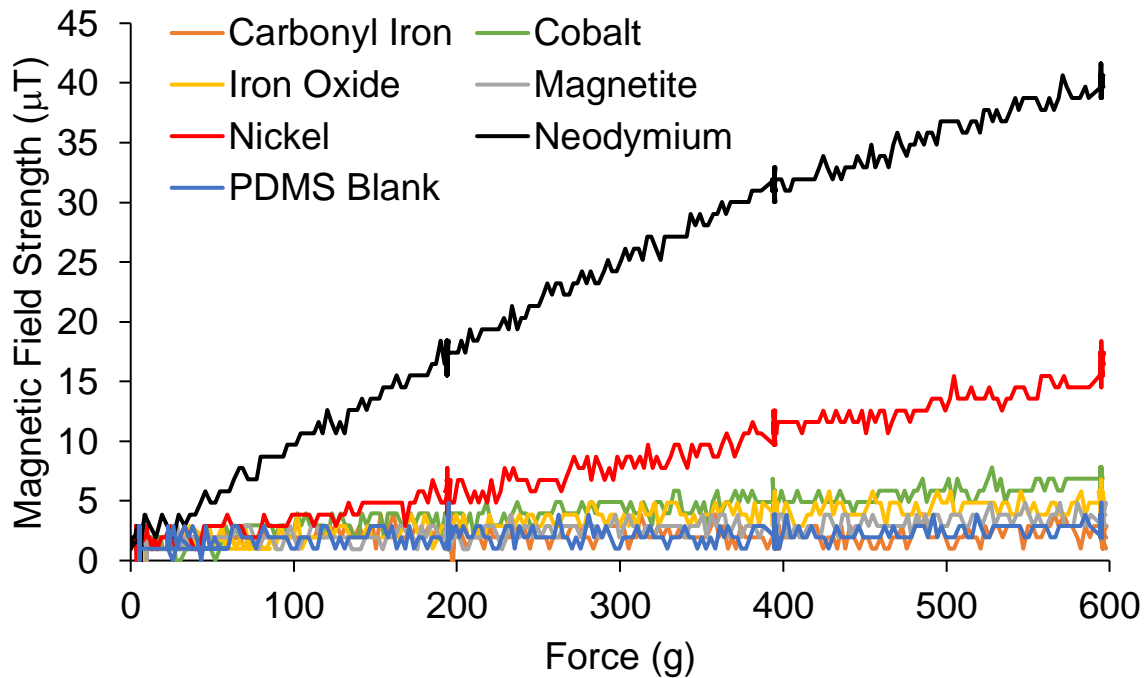


Figure 36: Magnetic field strength as a function of force for one sample (n=1) of each magnetic material at 1 wt % within PDMS. Only the compression cycles are displayed here.